Johann Wolfgang Goethe University
Frankfurt am Main

Department for theoretical physics

Master Thesis

Evolution of self-interacting dark matter subhalos

David Klemmer

January 2025

Submitted to

Prof. Dr. L. Sagunski

Department for theoretical physics
Goethe University Frankfurt a. M.

Dr. M. Fischer

University Observatory Munich
Ludwig Maximilian University of Munich

Abstract
This master's thesis investigates the evolution of satellite galaxies, focusing on the role of dark matter (DM) in shaping their development. Using high-resolution N-body simulations, the study qualitatively compares two DM models: cold, collisionless dark matter (CDM) and self-interacting dark matter (SIDM). While CDM successfully modeled large-scale structures of the universe, it faces challenges at smaller scales, particularly for satellite galaxies. SIDM, with its elastic scattering mechanism among DM particles, offers an alternative that modifies DM behavior on small scales while retaining CDM's large-scale successes.
The study uses the cosmological N-body code OpenGadget3 with a novel framework. In this framework, the host galaxy is modeled using an analytic potential, while self-interactions between the host's and satellite's DM particles are implemented through an evaporation scheme. This efficient framework allows detailed SIDM subhalo simulations and offers a foundation for future studies comparing simulations with observational data.
These idealized simulations are used to study the evolution of satellite galaxies and reveal that SIDM subhalos consistently experience greater mass loss than their CDM counterparts. Additionally, SIDM subhalo core evolution differs markedly from isolated SIDM halos, with mass loss accelerating evolution while tidal heating and evaporation slowing it down. As a result, the evolution strongly depends on the orbital parameters and the self-interaction cross-sections.

Zusammenfassung
In dieser Masterarbeit wird die Entwicklung von Satellitengalaxien untersucht, wobei der Schwerpunkt auf der Rolle der Dunklen Materie (DM) liegt. Mithilfe von hochauflösenden N-Körper-Simulationen vergleicht die Studie qualitativ zwei DM-Modelle: kalte, kollisionsfreie dunkle Materie (CDM) und selbst-wechselwirkende dunkle Materie (SIDM). Während sich CDM bei der Modellierung großräumiger Strukturen des Universums bewährt hat, stößt es bei kleineren Skalen, insbesondere bei Satellitengalaxien, auf Probleme. SIDM bietet mit seinem Mechanismus der elastischen Streuung zwischen DM-Teilchen eine Alternative, die das Verhalten der DM auf kleinen Skalen modifiziert und gleichzeitig die großräumigen Erfolge der CDM beibehält.
Die Studie verwendet den kosmologischen N-body code OpenGadget3 mit einem neuartigen Rahmenwerk. In diesem Rahmen wird die Wirtsgalaxie mit einem analytischen Potential modelliert, während die Selbstwechselwirkungen zwischen den DM-Teilchen des Wirts und des Satelliten durch ein Evaporationschema implementiert werden. Dieser effiziente Rahmen ermöglicht detaillierte SIDM-Subhalo-Simulationen, was eine Grundlage für zukünftige Studien bietet um Simulationen mit Beobachtungsdaten zu vergleichen.
Diese idealisierten Simulationen werden benutzt um die Entwicklung von Satelliten Galaxien zu studieren und zeigen, dass SIDM-Subhalos durchweg einen größeren Massenverlust erfahren als ihre CDM-Gegenstücke. Darüber hinaus unterscheidet sich die Entwicklung des SIDM-Subhalo-Kerns deutlich von der isolierter SIDM-Halos, wobei der Massenverlust die Entwicklung beschleunigt, während Gezeitenerwärmung und Evaporation sie verlangsamen. Infolgedessen hängt die Entwicklung stark von den Orbitalparametern und der Selbstwechselwirkungsquerschnitte ab.

Contents

1 Introduction

This master's thesis investigates the evolution of satellite galaxies, which orbit more massive host galaxies like the Milky Way. The focus of this thesis is on the role of DM in shaping their evolution. Their evolution is compared for two DM models: cold, collisionless dark matter (CDM) and self-interacting dark matter (SIDM). To achieve this, high-resolution N-body simulations provide a qualitative study of their structural evolution.

DM remains one of the greatest mysteries in modern physics. Observations, such as galaxy rotation curves and gravitational lensing, reveal that most of the Universe's matter is invisible. This unseen matter, termed DM, interacts primarily through gravity, but its true nature remains unknown.
The CDM model assumes that DM interacts only gravitationally. This model has achieved significant success in N-body simulations, which explore how the early universe evolved from small matter fluctuations to the large-scale structure we observe today [1]. These simulations show that small fluctuations grow over time due to the gravitational clustering of CDM particles, forming a giant web of matter filaments interspersed with voids. This web is known as the large-scale structure of the universe. Simulated large-scale structures closely match observed ones, validating the CDM model on cosmic scales [2].
One of the key predictions of CDM simulations is the hierarchical formation of DM structures. Within the large-scale structure, dense DM halos form, hosting galaxy clusters. These clusters contain smaller DM halos (galaxies), which themselves host even smaller DM subhalos (satellite galaxies) [3]. In these halos, baryonic matter accumulates, forming stars and other astrophysical objects. This process gives rise to the satellite galaxies, galaxies, and galaxy clusters we observe today. Each of these systems consists of a DM halo and baryonic components, such as stars and gas [4].
While CDM simulations excel at reproducing large-scale structures, discrepancies arise at smaller scales. For satellite galaxies, CDM simulations often overestimate the central density of some satellites while underestimating it for others. These discrepancies have motivated the development of alternative DM models, which aim to retain CDM's success on large scales while addressing its shortcomings on smaller scales. One such alternative is SIDM, which modifies DM behavior on small scales while preserving CDM's large-scale success [5, 6].

SIDM alters DM distribution through elastic scattering among DM particles. This scattering facilitates heat transfer and thermalization in a halo's inner regions. Initially, SIDM leads to a lower-density core (core-expansion phase). Over time, the core can collapse into a high-density center (core-collapse phase) [5]. How fast this evolution takes place depends on the interaction rate of the DM particles, which is characterized by the self-interaction cross-section per unit mass σ/m. To maintain consistency with CDM at large scales, the self-interaction cross-section in SIDM must decrease as system size increases. Observations across a range of systems—from satellite galaxies to galaxy clusters—support this behavior. For example, explaining the diversity of galaxy rotation curves requires a higher cross-section than allowed by constraints from galaxy clusters [7–10].
A notable feature of DM systems is the relationship between mass and velocity. Larger systems, which contain more mass, have particles with higher relative velocities compared to smaller systems.

For example, in clusters, DM particle velocity dispersions are $\sim 1000\,\mathrm{km/s}$, whereas in galaxies, they range from $\sim 1 - 100\,\mathrm{km/s}$. This trend suggests that the SIDM cross-section should decrease with increasing velocity to remain consistent with observations. Such velocity-dependent cross-sections allow for larger values (e.g., $\sigma/m \sim 1\,\mathrm{cm}^2/\mathrm{g}$) on galaxy scales while adhering to stricter constraints on cluster scales ($\sigma/m \leq 0.1\,\mathrm{cm}^2/\mathrm{g}$) [11–19].
On small scales, such as in satellite galaxies, high interaction rates can drive halos toward core collapse. This core collapse and the prior core expansion phase can explain the diversity of central densities observed in Milky Way satellite galaxies [20–28]. Core collapse, potentially unique to SIDM, has gained significant attention in recent research [29–38].

Satellite galaxies provide a valuable testing ground for DM models. Their significant discrepancies with CDM predictions make them ideal systems for studying DM models. Additionally, their high interaction rates in SIDM strongly influence their evolution, making them particularly useful for investigating SIDM [39].
To study DM in satellite galaxies, many surveys aim to obtain observational data. For instance, the Satellites Around Galactic Analogs (SAGA) survey [40] has identified several hundred satellite galaxies around Milky Way mass-like galaxies. The Gaia survey [41] has observed satellite galaxies in the Milky Way. Upcoming surveys, such as the Large Synoptic Survey Telescope (LSST) from the Vera Rubin Observatory [42], will provide even more data on Milky Way satellites. These observations enable detailed comparisons between simulations and observations on small scales.
Several observables can be used to compare simulations with observations of satellite galaxies. These include individual satellite properties, such as density, velocity profiles, the maximum circular velocity, as well as properties of satellite populations, like the spatial and mass distributions of satellites. Perturbations in gravitational lensing caused by satellite galaxies can be used to derive a projected mass and density slope of the satellite. Those perturbations in gravitational lensing require DM subhalos with high central densities, which CDM halos struggle to reproduce. SIDM halos in the core collapse phase could meet these constraints [43, 44].

Observations from surveys like SAGA, along with predictions from advanced N-body simulations such as "The Dark Side of FIRE" [45], underscore the complexity of satellite galaxies. While N-body simulations effectively model large-scale structures, simulating smaller systems like satellite galaxies remains challenging due to the extreme mass ratio between the satellite and the host system. This disparity makes it computationally expensive to model these systems in N-body simulations, which effectively limits the number of systems and DM models that can be simulated. The N-body simulations in this thesis are run using OpenGadget3 [46], which includes a SIDM scattering routine [47, 48]. Full N-body simulations, particularly for SIDM on small scales, are computationally intensive due to the high resolution required. To reduce these computational costs, this research uses an analytic potential to represent the host galaxy while resolving the satellite galaxy with particles. Virtual host particles, which are sampled from the host's density profile, are introduced to mimic the physical presence of host DM particles and enable the calculation of self-interactions between the satellite and host DM particles. This efficient framework enables detailed SIDM simulations with manageable computational demands.
Dynamical friction, the deceleration of a satellite galaxy due to momentum loss from gravitational interactions, is excluded from the model. This simplification is justified for satellite galaxies with masses much smaller than their host halos ($m_{\mathrm{sub}} \leq \frac{1}{1000} m_{\mathrm{host}}$) [49].

This N-body simulation framework was applied to qualitatively study the evolution of DM subhalos, yielding several key insights. First, SIDM subhalos consistently lose more mass compared to their CDM counterparts, with the difference becoming more pronounced under stronger tidal forces. Second, the core evolution of SIDM subhalos is significantly altered compared to isolated SIDM halos. Mass loss generally accelerates core evolution [21], whereas tidal heating and evaporation decelerate the overall core evolution and make this evolution highly dependent on the subhalo's orbital parameters and the self-interaction cross-section.

This thesis is structured as follows:
Chapter 2 recaps our knowledge of DM, from its discovery to the success of CDM on large scales and the crisis on smaller scales. The SIDM model is introduced as a potential solution, focusing on velocity-dependent cross-sections and the unique effects of SIDM on satellite evolution.
Chapter 3 discusses the already implemented numerical framework in OpenGadget3, including the gravitational and self-interaction routines for DM particles. The chapter also covers the generation of initial conditions (IC) using SpherIC and tests the framework on an isolated DM halo.
Chapter 4 presents the implemented framework of this thesis. The results are discussed from simulations of satellite galaxies on three characteristic orbits. Comparisons are made between CDM and SIDM models with different cross-sections, highlighting typical differences and SIDM-specific effects.
Chapter 5 discusses and evaluates the limitations of the framework.
Chapter 6 summarizes the thesis findings.
Chapter 7 suggests improvements for future work based on the discussion and limitations of the framework.

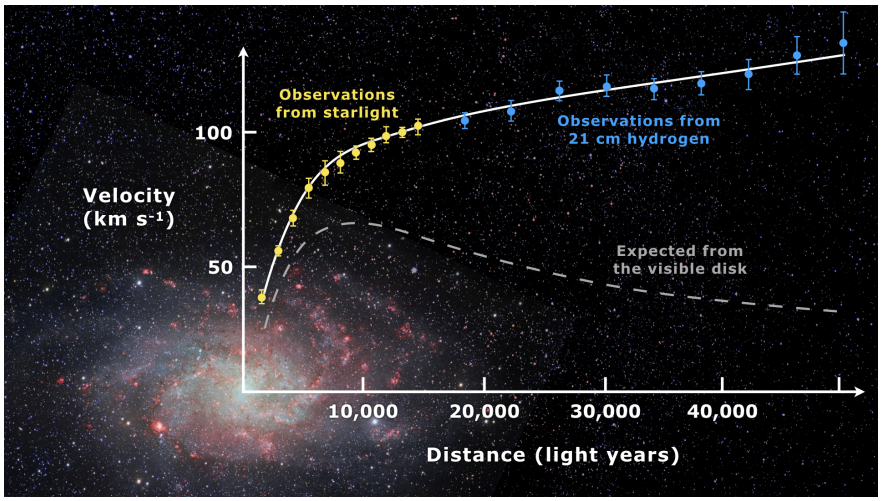

Figure 1: Rotation curve of spiral galaxy Messier 33 measured by starlight and 21-centimeter hydrogen line (yellow and blue points with error bars), and a predicted one from distribution of the visible matter (gray line). The discrepancy between the two curves can be accounted for by a DM halo surrounding the galaxy. [53]

2 Dark Matter

DM plays a central role in modern cosmology and astrophysics. Although its precise nature remains unknown, its gravitational influence is essential for explaining a wide range of astronomical observations. This chapter summarizes the discovery of DM, the development of the CDM model, and its success at large scales. This is followed by a discussion of the challenges CDM faces on smaller scales and introduces SIDM as a potential solution.

The first evidence suggesting the existence of DM emerged in the 1940s. Jon Oort analyzed the motions of stars within galaxies [50]. He observed that the visible matter was insufficient to explain the stars' observed velocities. This observation was an early indication that the mass we can see might not account for all the gravitational effects within galaxies.
The concept of DM was formally introduced by Swiss astronomer Fritz Zwicky in 1933 [51]. While investigating the Coma Cluster, Zwicky noticed that the galaxies in the cluster were moving much faster than expected based on visible mass alone. The gravitational force from only the visible matter could not keep the cluster bound. This implied the presence of additional, unseen mass. Zwicky termed this invisible mass "dunkle Materie" or "dark matter" and estimated that it accounts for most of the cluster's mass. However, his idea received little attention at the time.
In the 1970s, the concept of DM gained wider acceptance, largely due to the work of Vera Rubin and Kent Ford [52]. They observed spiral galaxies and found that stars in the outer regions of these galaxies orbited at unexpectedly high velocities. These velocities could not be explained by visible matter alone, providing strong evidence for the existence of DM on a galactic scale.

In figure 1 an example is shown for the discrepancy between expected and observed rotational

curves. This rotation curve belongs to the spiral galaxy Messier 33 [53].
The rotational curve assumes circular velocities around a spherically symmetric enclosed mass profile $M(r)$, which is described by:

$$v_{\text{circ}} = \sqrt{\frac{\mathrm{G}M(r)}{r}}. \tag{2.1}$$

The expected rotation curve is calculated based on the enclosed mass of visible matter. However, the observed rotation curve is significantly higher. Consequently, the enclosed mass derived from the observed rotation curve is much larger than the enclosed visible matter. This discrepancy is attributed to the presence of DM.
Such observations have led scientists to conclude that DM constitutes a significant portion of the Universe's total mass. While not all baryonic matter, such as stars or hot gas clouds, emits detectable light, some baryonic matter may remain unseen. However, constraints from Big Bang nucleosynthesis strongly limit the amount of baryonic matter that could account for DM. Observations of baryonic elements, such as protons, neutrons, and electrons, must align with the abundances predicted by nucleosynthesis. This alignment indicates that the majority of DM must be non-baryonic [54].

Figure 2: This composite image shows the galaxy cluster 1E 0657-56, also known as the "bullet cluster". This cluster was formed after the collision of two large clusters of galaxies. In red you see the baryonic gas clouds and in blue the astrophysical objects (stars, etc) and DM of both systems [55].

2.1 Cold Dark Matter

Despite limited knowledge about DM's nature, it is known to be non-baryonic and to exert a gravitational influence.
The Bullet Cluster, a collision of two galaxy clusters, provides a unique opportunity to study DM. In figure 2, two main components of the Bullet Cluster can be seen: one galaxy cluster on the left and another on the right (each cluster consists of a blue and red region). The red regions represent hot baryonic matter, observed through X-rays, while the blue regions represent astrophysical objects, including stars and DM. DM is detected indirectly via gravitational microlensing [55].
The baryonic matter clouds are located between the two clusters, while stars are distributed farther out. The baryonic matter clouds, having a high scattering cross-section, interact frequently and tend to clump together. In contrast, stars, with low scattering cross-sections, experience minimal interactions, allowing them to pass through each other with little disturbance. The galaxy clusters remain gravitationally bound and continue to orbit each other, while the baryonic matter clouds accumulate at the center due to frequent scattering events.
Microlensing observations reveal that DM aligns more closely with the path of the stars than with the baryonic matter clouds. This alignment suggests that DM particles must be collisionless, at least on the scale of galaxy clusters [56].

This understanding led to the development of the CDM model. In this model, DM particles are considered cold (non-relativistic velocities) and collisionless, interacting only through gravity.
The λCDM model [58], a cosmological framework, incorporates CDM and dark energy. It describes the expansion of the universe from the Big Bang to the present. The expansion rate of the universe

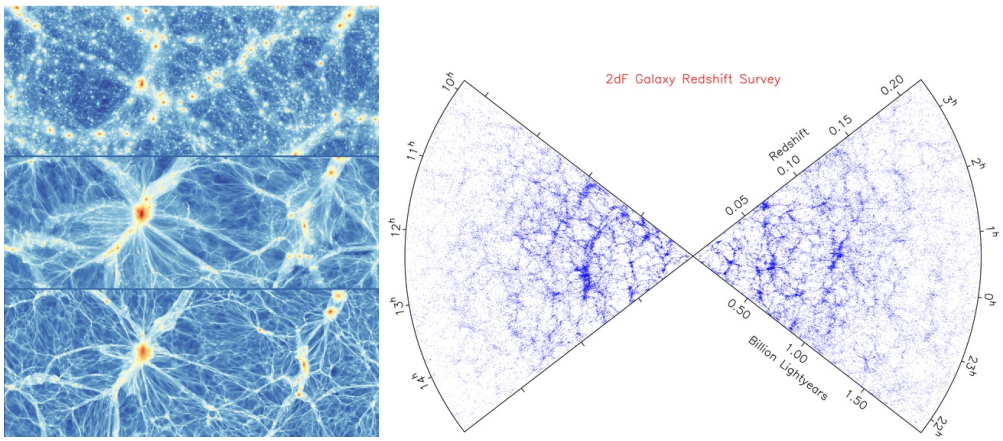

(a) (b)

Figure 3: (a) Large scale structures of our universe from λCDM N-body cosmological simulation [2].
(b) Observed large scale structures from the 2dF Galaxy Redshift Survey [57].

is described by the Hubble parameter $H(t) = \frac{\dot{a}}{a}$. a is the scale factor and describes the factor of how a given length in our universe has changed from the past/future to today. In other words, the factor a scales the expansion of our universe. By assuming an isotropic expansion (no preferred direction) and the Copernican principle (no place is special), the Friedmann-Lemaitre equation is derived from general relativity (GR) [59]:

$$H^2(t) = H^2(0)(\Omega_{r,0}a^{-4} + \Omega_{m,0}a^{-3} + \Omega_\Lambda + \Omega_{K,0}a^{-2}) \tag{2.2}$$

The current expansion rate of the universe is represented by $H(0)$. The universe's content today is described by three density parameters Ω. $\Omega_{r,0}$ represents the radiation content, $\Omega_{m,0}$ describes the matter content, which includes both baryonic matter and DM, and Ω_Λ accounts for the dark energy content. $\Omega_{K,0}$ represents the spatial curvature density. These density parameters collectively influence the expansion of the universe.
According to this model and based on nucleosynthesis arguments, dark energy accounts for roughly 70% of the universe's mass-energy density, while dark matter is estimated to contribute about 25%. Together, these two components constitute approximately 85% of the total matter content in the universe [59].
The ΛCDM model has been extensively utilized in cosmological N-body simulations [1] to investigate the evolution of the universe from its earliest observable state to the present day. These simulations begin at the epoch of the cosmic microwave background (CMB), which represents a snapshot of the universe approximately 380,000 years after the Big Bang. At this time, the universe had cooled enough for electrons and protons to combine into neutral hydrogen, allowing light to travel freely. This light, now observed as the CMB, reveals very small temperature fluctuations that correspond to density variations in the early universe. These variations reflect the initial distribution of matter and serve as the starting point for N-body simulations [1, 59].
Using observations of the CMB precise maps of these density fluctuations are generated. These maps are used as the IC for cosmological N-body simulations. The N-body simulations then evolve

these density perturbations over billions of years, under the influence of gravity and the expansion of the universe, as described by the ΛCDM framework. This process models the growth of structures through hierarchical clustering, where smaller structures form first and then merge to create larger ones, such as galaxies, galaxy clusters, and the vast cosmic web of matter.
The results of these simulations align remarkably well with observations of the large-scale structure of the universe, including the distribution of galaxies and galaxy clusters. Both simulations and observations show a web-like structure, indicating that the ΛCDM model successfully reproduces the universe's large-scale structure. This can be seen in figure 3. This consistency reinforces the validity of the CDM model on these scales and establishes cosmological N-body simulations as an essential tool for understanding the Universe's evolution [2, 59].
A key prediction of CDM simulations is the hierarchical organization of matter, with larger dark matter (DM) halos containing subhalos. Large-scale structures are composed of galaxy clusters, which host galaxies, and within these galaxies, smaller structures such as satellite galaxies are found [3]. However, at the scale of satellite galaxies, significant discrepancies arise between the predictions of ΛCDM simulations and observations. These discrepancies are collectively known as the "small-scale crisis" [5, 6].

The challenges on small scales have motivated the development of alternative dark matter models. These models aim to retain the successes of CDM at reproducing large-scale structures while addressing the discrepancies seen at smaller scales.

2.1.1 Small-scale crisis

There are four primary discrepancies between CDM N-body cosmological simulations and observations at small scales.

The first discrepancy is known as the core-cusp problem [5, 6, 60]. CDM simulations predict that the density of dark matter halos increases steeply toward their centers, forming a "cusp" density profile. However, observations of galaxy halos suggest a nearly constant central density, forming a "cored" density profile. This cored profile has a lower central density than the steep cusp predicted by CDM simulations.

The second issue is the diversity problem [5, 6, 61]. CDM simulations produce halos with highly uniform density profiles for a given halo mass. In contrast, observations of galaxies reveal a much wider diversity in their density profiles. For example, some observed galaxies exhibit steep central densities resembling cusps, while others display flatter, core-like profiles. This diversity cannot be explained by CDM simulations alone, as they tend to overestimate the central density of some halos while underestimating it in others.

The third discrepancy is called the missing satellite problem [5, 6, 62]. CDM simulations predict that within a host halo, such as that of the Milky Way, there should exist a large number of smaller subhalos. For example, simulations estimate that the Milky Way should contain between 100 and 1000 subhalos, observations have identified only around 10 to 20 satellite galaxies.

The fourth discrepancy is the too-big-to-fail problem [5, 6, 63]. In the Milky Way, the most luminous satellite galaxies are expected to reside in the most massive subhalos, as these massive halos should have enough gravitational binding to retain gas and form stars. These subhalos, considered "too big to fail" in forming stars, should host observable satellite galaxies. However, CDM simulations predict that these massive subhalos are too dense in their central regions compared to observations. The observed satellite galaxies do not match the predicted density profiles of these subhalos, implying that either the central densities of massive subhalos are overestimated in simulations or that some mechanism prevents star formation in these "too-big-to-fail" halos.

Originally, these discrepancies were identified in DM-only simulations. Therefore, one possible solution involves incorporating dissipative baryonic processes (radiative cooling, star formation, supernova/active-galactic-nuclei (AGN) feedback, gas accretion, ...) to address these small-scale issues [64, 65]. Alternatively, these problems could be resolved by considering an alternative DM model that modifies CDM predictions at small scales. A promising candidate in this regard is SIDM [5, 6].
It seems plausible that a combination of baryonic matter and an alternative DM model is needed to consistently solve all the "small-scale crisis".

2.2 Self Interacting Dark Matter

The SIDM model assumes that DM particles not only exert a gravitational effect but can also self-interact through scattering processes. These self-interactions can be classified into two types: elastic and inelastic.
In this thesis, we focus on elastic scattering through $2 \rightarrow 2$ interactions. In elastic scattering, particles exchange momentum and energy without any net loss of either quantity. This process drives the thermalization of the halo, enabling the redistribution of kinetic energy and momentum among the DM particles.

2.2.1 Theoretical model of elastic scattering

The likelihood of scattering events and the distribution of scattering angles is governed by the differential cross-section, $\frac{d\sigma}{d\Omega}$, which depends on the scattering angle θ. This parameter quantifies the probability of scattering occurring at a specific angle.

The scattering angle significantly influences the transfer of momentum and energy between particles. Large-angle scattering results in a substantial exchange of momentum and energy between particles, whereas small-angle scattering involves smaller exchanges. Consequently, small-angle scattering typically requires a higher frequency of interactions to achieve a momentum or energy exchange comparable to that of large-angle scattering. Therefore, small-angle scattering is often called frequent scattering, and large-angle scattering is often called rare scattering [47].

A common particle physics model for SIDM is the Yukawa [5, 66] interaction, where a mediator particle facilitates the scattering. The mass of this mediator determines the angular dependence of the interaction. The differential cross-section for the Yukawa interaction is given by:

$$\frac{d\sigma}{d\Omega} = \frac{A}{((\alpha m)^2 + 4p^2 \sin^2(\frac{1}{2}\theta))^2} \tag{2.3}$$

A is a proportionality constant, α is the interaction coupling constant, m is the mass of the mediator, p is the relative momentum of the interacting particles and θ is the scattering angle.
The mediator mass plays a key role in defining the angular dependence. When the mediator mass is large ($\alpha m \gg 2p\sin(\frac{\theta}{2})$), the angular dependence becomes negligible, leading to an isotropic cross-section.
When the mediator mass is small, the Yukawa interaction exhibits a strong angular dependence, favoring small-angle scattering.

2.2.2 Isolated DM halo evolution

This chapter discusses the stability of CDM halos [67] and their evolution when elastic self-interactions between dark matter particles are introduced [5]. By understanding the gravitational equilibrium of CDM halos, we provide insights into the transitions from stable CDM halos to the

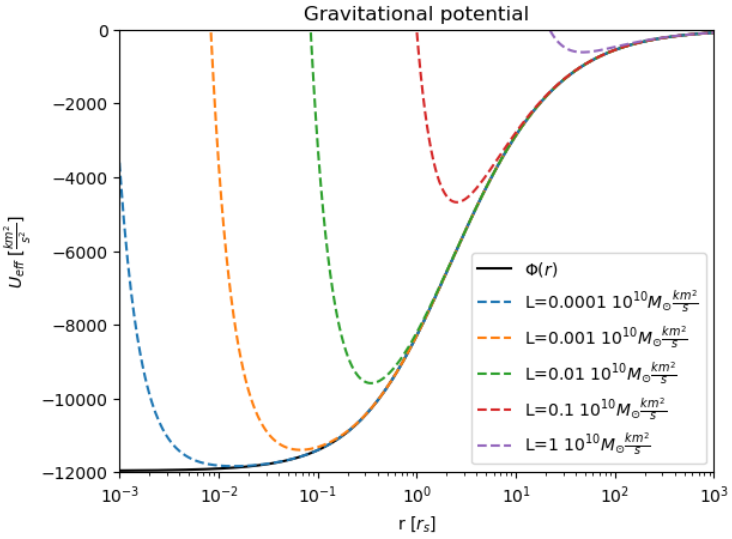

Figure 4: Gravitational potential $\Phi(r)$ (black) and effective potentials U_{eff} (blue, orange, green, red, and purple) for a particle with angular momentum L inside a CDM halo.

phases of core expansion and core collapse in SIDM halos.

CDM halos are self-gravitating systems [68]. Self-gravitating systems are constituted out of many massive objects. Those massive objects exhibit gravitational forces between them. At a sufficient density, this allows the system to hold itself together. All massive objects therefore need to be bound to the gravitational potential. By taking a look at the gravitational potential of a CDM halo (in figure 4), one sees that the potential $\Phi(r)$ has a deep well. A massive object is considered to be bound if its kinetic energy E_{kin} does not exceed the height of the well. This means that the kinetic energy of a bound particle must be lower than the potential energy $E_{\text{kin}} < |\Phi(r)|$. Then the particle cannot escape the gravitational pull. All bound particles therefore need to have less kinetic energy than potential energy. This results in a negative total energy $E < 0$ for self-gravitating systems. The effective potentials for a particle with a given angular momentum L are shown in figure 4 by the colored dashed lines. These lines indicate the regions where a particle with a specific angular momentum remains bound to the DM subhalo.
CDM halos are in gravitational equilibrium. This means that CDM halos are stable systems with no average structural changes over time. In those systems, the density and velocity distribution remain averaged unchanged over time. As the gravitational potential arises from the density distribution, this potential is also averaged unchanged. The virial theorem describes the gravitational equilibrium of self-gravitating systems. According to this theorem [68], a self-gravitating system is in equilibrium when the total kinetic energy (T) is half the total gravitational potential energy (U):

$$2T + U = 0 \tag{2.4}$$

This equation results in an overall negative energy $E = T + U = -T < 0$, as we expected it for a bound system, and is given for a CDM halo.
This section discusses how gravitational equilibrium is achieved by examining how the density

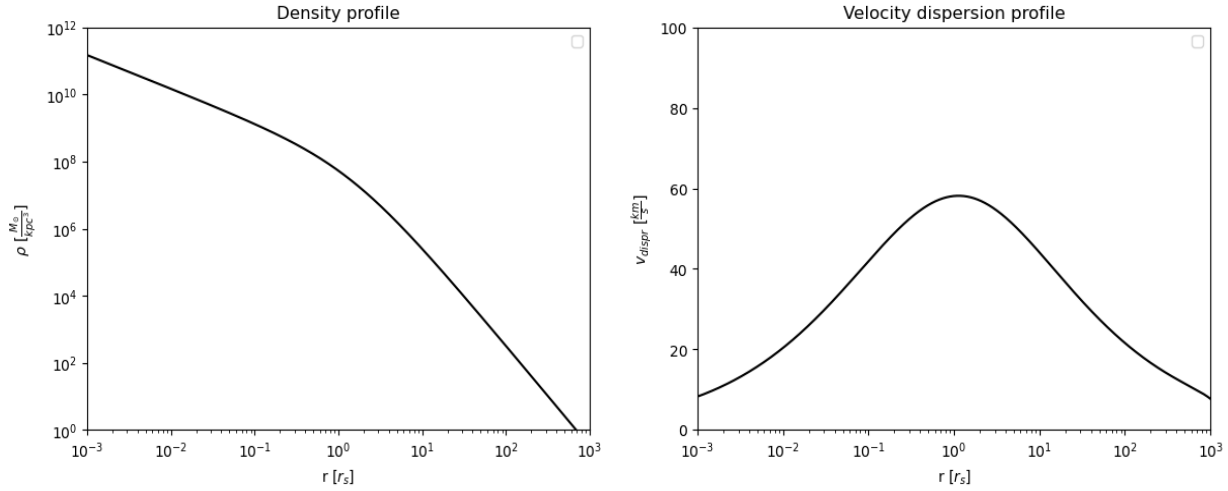

(a) (b)

Figure 5: (a) Density profile of the analytic NFW model, as described by equation (2.5). (b) Velocity dispersion profile corresponding to the analytic NFW model.

distribution shapes the gravitational potential and how the velocity dispersion counteracts the inward pull from the gravitational potential. The gravitational potential arises from the density profile. The density profile of a CDM halo has been identified from cosmological ΛCDM N-body simulations. Through all scales (from galaxy clusters to dwarf galaxies) the density profile can be characterized by two parameters: the scale density ρ_s and the scale radius r_s. This profile, known as the Navarro-Frenk-White (NFW) profile [69], is defined by the formula:

$$\rho(r) = \frac{4\rho_s}{\frac{r}{r_s}(1+\frac{r}{r_s})^2} \tag{2.5}$$

Gravitational equilibrium in a CDM halo can be understood as the balance between the gravitational inward pull and the outward centrifugal force acting on a particle. The gravitational force is given by $F_{\text{grav}} = -\frac{d\Phi}{dr}$, which depends on the gradient of the gravitational potential Φ, and the centrifugal force is $F_{\text{centri}} = \frac{mv_\perp^2}{r}$, where $v_\perp$ is the perpendicular velocity of the particle. On average, this perpendicular velocity is described by the velocity dispersion. Consequently, the velocity dispersion is closely related to the gradient of the gravitational potential.

The density profile at small radii declines weakly as $\rho(r) \propto r^{-1}$. This results in a deep gravitational potential with a vanishing central gradient. As a consequence, the velocity dispersion approaches zero at the center. The central region is therefore characterized by very high density and low velocity dispersion, making it both cold and dense.

Around the scale radius r_s, the density decreases more steeply, following $\rho(r) \propto r^{-2}$. The gravitational potential gradient reaches its maximum in this region, leading to the highest velocity dispersion. This intermediate region is less dense compared to the core but exhibits higher particle velocities, making it relatively "hot".

At large radii, the density declines sharply as $\rho(r) \propto r^{-3}$, resulting in a decreasing gradient of the gravitational potential. Correspondingly, the velocity dispersion also decreases outward. The outer

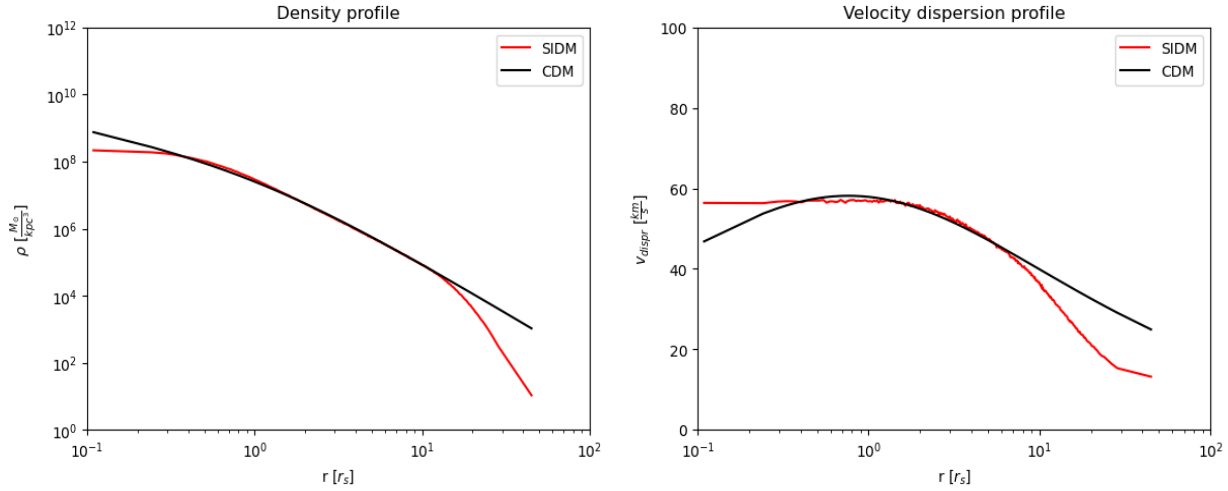

(a) (b)

Figure 6: Density (a) and velocity dispersion (b) profile of a SIDM halo with maximum core size (red) compared to the analytic NFW profile (black).

region of the halo is characterized by very low density and low particle velocities, making it cold and diffuse.
The overall density profile and corresponding velocity dispersion of a CDM halo are intricately linked to maintain gravitational equilibrium. Figure 5 illustrates this relationship.

Introducing elastic scattering between DM particles leads to thermalization within the halo. Thermalization is the process of reaching a thermal equilibrium. This is achieved through heat flow from the hotter to the colder region, which heats the colder region until a constant temperature is reached. The elastic scattering redistributes kinetic energy between the particles, which drives the thermalization [5, 6].
The temperature gradient indicates the direction of the heat flow. The velocity dispersion is proportional to the temperature. Therefore we can identify the temperature gradients inside the halo with the velocity dispersion profile. The velocity dispersion gradient is positive in the inner region (center to r_s) and negative in the outer region (r_s outward). This results in heat flow from r_s inwards and outwards. High densities lead to higher scatter probabilities. Due to the outward decreasing density, the scattering probability is greater inward. This causes energy to flow first mainly inward along the positive gradient. This inward kinetic energy transfer heats the inner region, which results in larger velocities in this region. As particles in the inner region reach higher velocities, those particles diffuse outward. This reduces the central density and results in a gravitational potential that is shallower and less binding. This results in a constant central density. This constant central density is called the core. This process continues until the positive temperature gradient vanishes and a uniform temperature is reached within the central region. At this point, the SIDM subhalo has reached its maximum core size. The corresponding density and velocity dispersion are shown in figure 6. This phase of the evolution is called the core expansion phase and is caused by the thermalization of the inner halo [5, 6].

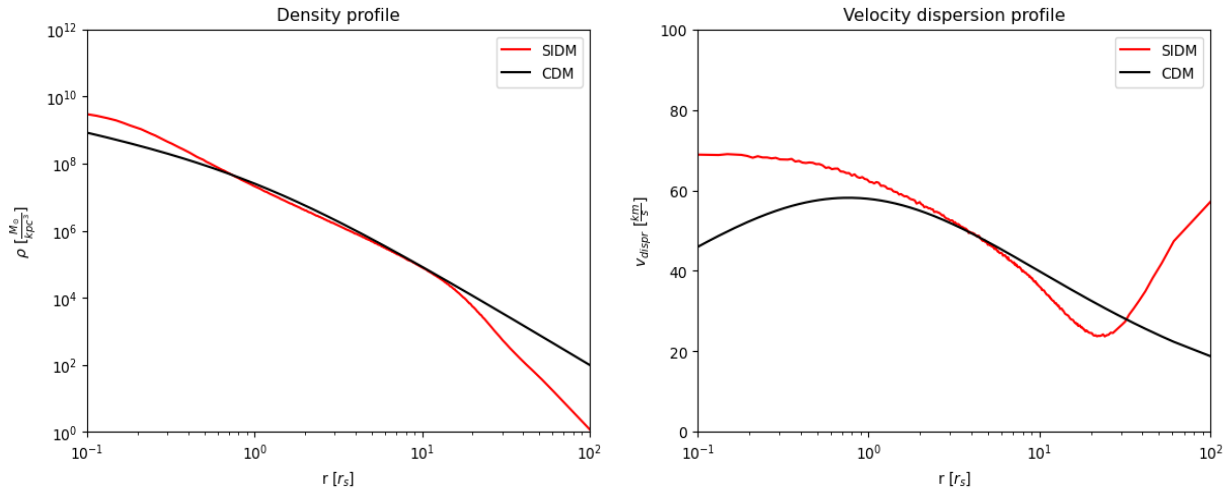

(a) (b)

Figure 7: Density (a) and velocity dispersion (b) profile of a SIDM halo in core collapse phase (red) compared to the analytic NFW profile (black).

Once the core reaches its maximum size, the overall temperature gradient in the halo becomes negative. The heat of the halo can now only flow outwards. This results in kinetic energy loss from the core to the outer regions. The particles, deprived of kinetic energy, begin to fall inwards. The halo begins to collapse under its gravity. This initiates the core collapse phase and results in an increase in the central density. The increase of the central density deepens the potential well. As particles fall inward, they accelerate. Due to the deeper gravitational potential, they accelerate even stronger, resulting in even higher velocities. This change in the density and velocity dispersion profile is shown in figure 7. The temperature in the core rises, breaking the uniformity established during core expansion, and the negative temperature gradient becomes larger. This enhanced temperature gradient accelerates energy loss to the outer regions, driving the collapse further and faster. Over time, the central density surpasses its initial value in the CDM state, and the central temperature and density continue to grow without limit [5, 6].
These two phases of core evolution—core expansion and core collapse—provide a unified framework for addressing the core-cusp problem and the diversity problem observed in the density profiles of Milky Way-mass galaxies and their satellite systems [20–28].

The core collapse phase exhibits an intriguing thermodynamic behavior. The core's temperature and velocity dispersion increase despite losing energy to the outer regions. This counterintuitive result arises from the negative heat capacity of self-gravitating systems.
The total energy (E) of a self-gravitating system has to be negative. From the virial theorem we know the total energy is the negative kinetic energy, which can be connected to the mean temperature of the system [68]:

$$E = -T = -\frac{1}{2}m < v^2 >= -\frac{3}{2}Nk_B\bar{T} \tag{2.6}$$

The heat capacity (C) is defined as the derivative of the total energy with respect to the mean temperature ($\bar{T}$):

$$C = \frac{dE}{d\bar{T}} = -\frac{3}{2}Nk_B < 0 \tag{2.7}$$

This negative heat capacity implies that when the system loses energy ($dQ < 0$), it heats ($d\bar{T} = \frac{dQ}{C} > 0$). The increase in temperature (larger temperature gradient) leads to faster energy loss, driving a feedback loop that further accelerates the collapse. If energy is injected ($dQ > 0$) into the system, the system cools down $d\bar{T} < 0$ [68].

A less massive SIDM halo evolves more rapidly than a more massive one due to its shallower gravitational potential, which allows energy to transfer more efficiently throughout the halo. In a shallower potential, particles are less tightly bound, enabling faster heat flow inward during the core expansion phase and more rapid energy loss outward during the core collapse phase, leading to quicker structural changes.
The concentration of the halo also plays a significant role in its evolution. A more concentrated halo has a steeper density profile and a deeper central potential, which slows down the redistribution of energy. In contrast, a less concentrated halo with a flatter density profile exhibits a shallower potential, accelerating the processes of core expansion and collapse. Thus, both lower mass and lower concentration contribute to faster internal evolution in SIDM subhalos [70].

2.2.3 Velocity-dependent cross-section

As discussed in chapter 2.1, DM particles must have very small or vanishing cross-sections on large scales to explain the Bullet Cluster and the formation of the large-scale structures.
However, as discussed in chapter 2.1.1 and 2.2, SIDM could potentially resolve several small-scale issues but would require a sufficiently larger cross-section than what is observed on large scales.
This can be realized for SIDM by implementing a velocity-dependent cross-section.

The velocity-dependent self-interaction cross-section per unit mass σ_T/m quantifies the intrinsic likelihood of scattering events between DM particles.
Typically, this velocity dependence is expressed for a momentum transfer cross-section. It is derived from the differential cross-section $\frac{d\sigma}{d\Omega}$. The momentum transfer cross-section is defined as [47]:

$$\sigma_T = 2\pi \int \frac{d\sigma}{d\Omega}(1 - |cos\theta_{\text{cms}}|)dcos\theta_{\text{cms}} \tag{2.8}$$

The resulting velocity-dependent cross-section is then [72]:

$$\frac{\sigma_T}{m} = \frac{\frac{\sigma}{m}}{(1 + (\frac{v}{w})^2)^2} \tag{2.9}$$

w is a characteristic velocity scale that determines how rapidly the cross-section decreases as velocity increases. This is sometimes referred to as a "width" parameter. v is the relative velocity between two particles of the interaction. σ is the cross-section for the limit $v \ll w$.
However, in real astrophysical systems, the effective cross-section per unit mass σ_{eff}/m determines

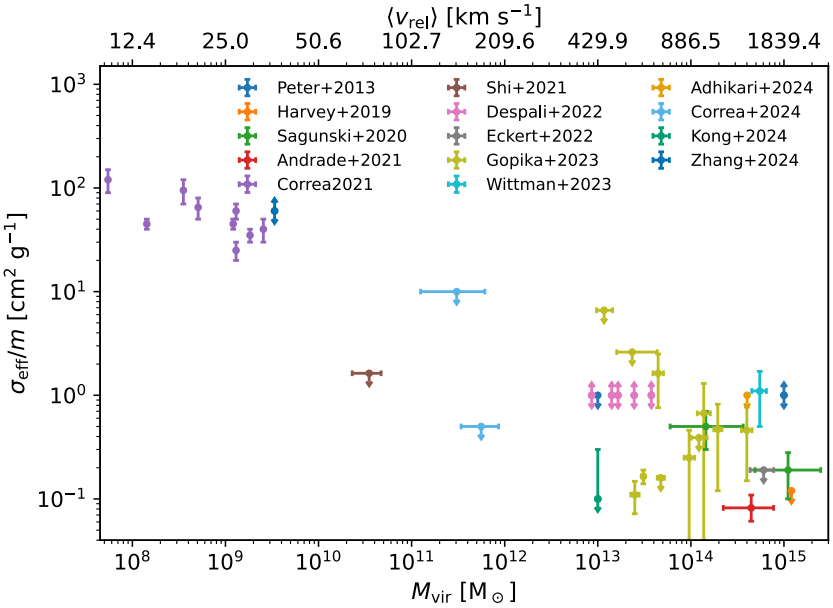

Figure 8: Constraints on the effective cross-section for different mass-sized systems [71].

the actual scattering probability in a given environment and depends on the relative velocities v_{rel} of DM particles in that system [72].

$$\frac{\sigma_{\text{eff}}}{m} = \frac{\langle v_{\text{rel}}^5 \frac{\sigma_T}{m} \rangle}{\langle v_{\text{rel}}^5 \rangle} \tag{2.10}$$

This effective cross-section is particularly relevant because different systems, such as satellite galaxies and galaxy clusters, exhibit a wide range of typical relative particle velocities, directly influencing the interaction rate for any given value of σ_T/m. A significant observation is that scattering velocities typically scale with halo mass. Larger halos, with more mass, contain particles with higher relative velocities. An overview of constraints on the effective cross-section for different systems is shown in figure 8. From those constraints, it can easily be seen that the scattering probability decreases for more massive systems (for larger relative velocities). Systems with a high effective cross-section are of particular interest because SIDM significantly influences their evolution. Satellite galaxies are important for studying SIDM, as they offer valuable insights due to their high effective cross-section.

2.2.4 DM subhalo evolution

The hierarchical structure formation predicted by ΛCDM cosmology suggests that DM halos host substructures known as DM subhalos [3].
DM subhalos typically form as isolated DM halos in the early Universe before merging with larger systems. During their orbital journey, they cross the virial radius of a host halo and become gravitationally bound. The properties of subhalos at the time of infall, such as their mass, concentration,

and orbital parameters, exhibit statistical variation. Once bound, subhalos experience external dynamical effects that alter their structure and behavior compared to their isolated counterparts (2.2.2). Those effects are tidal forces and heating, evaporation, and dynamical friction.
CDM subhalos are only affected by tidal forces and dynamical friction due to their collisionless particles [23]. Among these effects, tidal forces from the host system play the dominant role in shaping the subhalo's evolution.
Tidal forces arise from the gradient of the gravitational potential by the host system. This gradient varies across the subhalo. Particles closer to or farther from the host center experience varying gravitational pulls. These varying forces stretch the subhalo, elongating its structure along the direction of the host's gravitational field.
When the tidal force on a particle exceeds the subhalo's gravitational force, the particle becomes unbound, leading to mass loss. This effect is most pronounced in the outer regions of the subhalo, where gravitational binding is the weakest. The stripped particles are not lost randomly; instead, they form tidal streams that trail and precede the subhalo along its orbit around the host galaxy.
The inner regions of the subhalo, where the gravitational binding is stronger, are more resistant to tidal forces. These central regions typically retain their cuspy density profile, characteristic of CDM subhalos. However, if the subhalo passes too close to the host's center, where tidal forces are most intense, it may experience total disruption, losing all its bound mass and effectively dissolving [73].
The second effect acting on the CDM subhalo is dynamical friction. Dynamical friction results from the gravitational interaction between the subhalo and the surrounding host's dark matter particles. As the subhalo moves through the host halo, it exerts a gravitational pull on the surrounding particles, causing them to cluster behind the subhalo. This cluster of particles creates a drag force opposite to the subhalo's motion, leading to a gradual loss of orbital energy and causing the subhalo to spiral toward the host's center. This process is known as orbital decay.

SIDM subhalos experience additional effects due to self-interactions between dark matter particles: tidal heating and evaporation [49, 74]. The presence of a core in SIDM subhalos makes the particles less gravitationally bound. This becomes more pronounced as the core size grows. Tidal forces can therefore strip particles more efficiently and lead to an increasing mass loss compared to CDM. As the subhalo loses mass, it's internal evolution is accelerated compared to the corresponding isolated SIDM halo [21].
In addition to tidal forces, the SIDM subhalo can also experience tidal heating. Particles, which get stripped away from tidal forces, are accelerated to higher velocities. If those tidal forces are strong enough, they can create a positive temperature gradient in the outer regions of the subhalo. In contrast to CDM subhalos, where this kinetic energy disperses outward as the particles are stripped away, SIDM halos can redistribute the kinetic energy inward through self-interactions. This redistribution of kinetic energy heats the inner halo, causing particles from the central region to disperse outward. This dispersion reduces the central density and the gravitational potential becomes shallower, which unbinds high-velocity particles from the central region. This process effectively lowers the temperature in the inner halo. Tidal heating thus initiates a core expansion phase (positive temperature gradient), which may expand the core further, interrupting or delaying a core-collapse phase. Thus slowing down the internal evolution [49, 74].
The injection of kinetic energy through tidal heating paradoxically leads to a cooling of the SIDM halo. As discussed earlier in the context of self-gravitating systems, the negative heat capacity

implies that energy input results in a decrease in temperature [68].

Another unique effect in SIDM subhalos is evaporation, which occurs through elastic scattering between subhalo and host particles. Typically, this scattering accelerates subhalo particles to velocities high enough to escape the subhalo's gravitational pull, resulting in mass loss for the subhalo. This evaporation scattering occurs particularly in the dense central regions, where scattering probabilities are highest. By reducing the central density, evaporation shallows the gravitational potential, which unbinds high-velocity particles from the core. By reducing the central velocity dispersion, evaporation maintains a positive temperature gradient, which suppresses the core collapse. Thus extending the overall internal evolution. The likelihood of evaporation scattering can be reduced by implementing a velocity-dependent cross-section. Relative velocities within the subhalo are typically lower than those in the host halo. As a result, the evaporation scatter rate is reduced more than the scattering rate within the subhalo itself. This balance allows core-collapse phases to persist for a subhalo experiencing evaporation. As evaporation leads to mass loss in the central region, it leads to a shallower gravitational potential. This also accelerates the internal evolution compared to the corresponding isolated SIDM halo [49, 74].

3 N-body simulations

This thesis uses N-body simulations to investigate the evolution of subhalos. This chapter discusses the already implemented framework from OpenGadget3, which serves as the starting point for the study. The focus is on modeling gravitational interactions and elastic self-interactions between DM particles. Additionally, the process of generating the IC for the subhalo using SpherIC is explained. These IC are then used to simulate isolated CDM and SIDM halos, testing the already implemented framework from OpenGadget3 and the IC from SpherIC.

3.1 OpenGadget3

The simulations in this thesis run with the N-body code OpenGadget3 [46]. OpenGadget3 is a successor to the code Gadget, which is an acronym for "Galaxies with dark matter and gas interactions". OpenGadget3 simulates gravitation and hydrodynamics between N bodies.
The term "N-body" refers to the fact that the system consists of N interacting bodies or particles. These particles do not correspond to individual physical particles, like atoms, but instead are representative elements. In the context of our DM simulations, each N-body represents a clump of DM rather than a single DM particle. Each N-body is called a numerical particle and represents multiple physical particles. Those N-body simulations calculate physical forces (for example, gravity) between all N-bodies and identify the resulting motion for each body.
OpenGadget3 contains many modules with additional physics such as: star formation, stellar/black hole feedback, magnetic hydrodynamics, thermal conduction, cosmic rays, and SIDM [47, 48].
For the simulations in this thesis, gravitation and SIDM are used: Those features of OpenGadget3 will be discussed in the following paragraphs.

3.1.1 Gravitation

OpenGadget3 handles gravitation via Newtonian physics. The gravitational acceleration of one numerical particle i due to another numerical particle j is defined as:

$$\vec{a_i} = \mathrm{G}\frac{m_j}{r_{ij}^3}\vec{r_{ij}} \tag{3.1}$$

G is the gravitational constant.
The total gravitational acceleration of a numerical particle i in the N-body simulation could be computed by summing over all gravitational accelerations from the $N-1$ particles. This is computationally expensive.
In OpenGadget3, gravity is treated through a hierarchical method known as the Tree algorithm, which efficiently calculates the gravitational forces between numerical particles. The Tree algorithm groups distant numerical particles into hierarchical "nodes" and calculates their combined gravitational effect as a single entity. This approximation is based on the angular size of the node as seen by a particle. Specifically, nodes that appear under a larger angle (relative to a fixed "opening angle") are further opened, and their constituent numerical particles are considered individually.

This adaptive criterion ensures that the computation focuses on precise interactions for nearby numerical particles while approximating the influence of distant groups to save computational resources. It is worth noting that the opening criterion is not solely a fixed angle but also accounts for the acceleration induced by the node. This refinement helps maintain accuracy in the force calculations [46].
A critical aspect of gravitational force computation in N-body simulations is the use of a softening length. The gravitational potential of a point mass is singular, leading to unrealistically large accelerations when numerical particles come very close to one another. The softening length introduces a smoothing factor to the gravitational potential, effectively preventing such singularities. This modification ensures that the gravitational forces remain finite at small separations and leads to more stable and realistic simulations [46].
By employing the Tree algorithm with softening, OpenGadget3 achieves a balance between computational efficiency and accuracy, making it particularly well-suited for studying the evolution of DM structures and satellite galaxies. The adaptive nature of the Tree method allows it to handle the wide range of densities encountered in cosmological simulations, from sparse outer regions to dense cores of DM halos. For a detailed discussion of these methods, the paper [75] provides a comprehensive overview of the underlying principles and their implementation in N-body codes.

3.1.2 Self-interacting dark matter

The SIDM module assumes elastic scattering, which conserves energy and momentum. This allows the calculation of post-scattering velocities based on the conservation laws.
This SIDM module is divided into two steps. Step one is about defining if two particles will scatter. If those particles scatter, step two is about calculating the post-scattering velocities.
Step one is implemented in a Monte Carlo scheme. This is done by considering a pair of particles within an interaction radius. Each pair of particles has an associated probability of interaction. A random number is generated for each pair, and if this random number is smaller than the calculated interaction probability, the particles scatter. This probabilistic approach ensures that the scattering process captures the statistical behavior expected in SIDM systems [47, 48, 72].
The probability of interaction between two particles is discussed now. First, consider a simple case where a single particle moves v through a constant density ρ. The particles of the constant density are at rest. The probability that the single particle scatters in a given time t is given by [47]:

$$P = \frac{\sigma}{m}\rho v t \tag{3.2}$$

For numerical calculations, the interaction probability for a single scatter event is needed. The equation (3.2) can exceed an interaction probability of 1, which corresponds to multiple scatter events. This restricts the interaction probability to $P \ll 1$ by choosing small enough time steps t.
In OpenGagdet3 the scattering is simulated between two numerical particles. A numerical particle represents many physical particles. The DM density distribution within a numerical particle is defined by a kernel function.

$$\rho_i(\vec{x}) = m_i W(|\vec{x} - \vec{x_i}|, h_i) \tag{3.3}$$

$W(|\vec{x} - \vec{x_i}|, h_i)$ is the kernel function, which depends on the kernel size h_i. An important property of the kernel function is that its volume integral yields exactly to 1. m_i is the mass of the numerical

particle [47].
If two numerical particles are within an interaction radius, the degree of the overlap of their DM density distribution quantifies the probability of interaction. The integration over two kernel functions of numerical particle i and j gives the kernel overlap Λ_{ij}. The kernel overlap determines to what degree the kernel functions of the numerical particles intersect and quantifies the probability of interaction. Based on this kernel overlap Λ_{ij}, the self-interaction cross-section σ/m and the relative velocity of the numerical particles $\Delta\vec{v_{ij}}$, the probability of interaction between two numerical particles i and j is given by:

$$P_i = \frac{\sigma}{m} m_j |\Delta\vec{v_{ij}}| \Delta t \Lambda_{ij} \tag{3.4}$$

The time step Δt needs to be kept small to ensure $P \ll 1$.
If two numerical particles are to scatter within the time interval Δt, the process is determined probabilistically. A random number x is drawn from a uniform distribution between 0 and 1. If $x \leq P$, the two numerical particles undergo a scattering event.

The calculation of the post-scattering velocities is discussed now. The post-scattering velocities are calculated in two different ways implemented by the modules rare SIDM (rSIDM) and frequent SIDM (fSIDM) [47, 48, 72].
First we consider rSIDM, which is analogous to the scattering of physical particles in the center-of-mass frame. The change of the velocity happens in a random direction $\vec{e}$. This is a unit vector, which depends on the scatter angle θ and an angle ϕ. The scattering angle θ is determined stochastically from the differential cross section. The angle ϕ is randomly chosen from a uniform distribution over the range $[0, 2\pi]$. If the particles have equal masses ($m_i = m_j$), their velocities in this frame are exactly opposite to each other. The post-scattering velocities are then calculated in the center-of-mass frame by [47, 72]:

$$\vec{v}_{i/j}^{\,\text{new}} = \frac{(\vec{v}_i + \vec{v}_j)}{2} \text{ +/- } \frac{\Delta\vec{v}_{ij}}{2}\vec{e} \tag{3.5}$$

Those post-scattering velocities are transformed back into the simulation's rest frame.
rSDIM is used for an isotropic cross-section in this thesis, but it can be implemented with any differential cross-section. For small angle scattering, rSIDM becomes very expensive computationally. Therefore, an additional SIDM module for calculating the post-scattering velocities is implemented. This module is called fSIDM and models efficiently small angle scattering.
Small angle scattering exchanges only a small amount of momentum and kinetic energy. Therefore the velocities change only slightly for fSIDM. The scattering is realized by applying a drag force. The drag force acts in the direction of the relative velocity Δv_{ij} and changes the velocity by $\Delta\vec{v}_{\text{drag}}$ [47, 72].

$$\vec{v}^{\,*}_{i/j} = \vec{v}_{i/j} \text{ -/+ } \Delta\vec{v}_{\text{drag}} \tag{3.6}$$

The lost energy from this drag force is then re-added as a velocity to the particle to ensure conservation of energy. This velocity is added in a random direction, but perpendicular to the direction of motion to correctly model the transverse momentum diffusion.

$$\vec{v}_{i/j}^{\,\text{new}} = \vec{v}^{\,*}_{i/j} \text{ +/- } \Delta\vec{v}_{\text{rand}} \tag{3.7}$$

This is symmetrically done for both numerical particles (i and j) to ensure conservation of energy and momentum.

The implementation of SIDM into OpenGadget3 can simulate multiple scattering events per particle within a single time step and handle any angle-dependency.

3.2 Initial Conditions

This paragraph is about generating the IC for the satellite galaxy. We focus for this thesis only on the DM properties of the satellite galaxy. The DM part of a galaxy is called a DM halo. DM halos are commonly described by an NFW profile as briefly discussed in chapter 2.2.2.

3.2.1 Navarro-Frenk-White profile

From cosmological N-body simulations with CDM, models for the spatial mass distribution of DM halos were designed. The NFW profile describes such halos and is commonly used to describe and simulate DM halos [69].
NFW halo density profile is defined as a function of the radius r in units of the scale radius r_s and can be written as in equation (2.5). This profile is characterized by two parameters: r_s and ρ_s. Those two parameters need to be identified for the halo under consideration.
The scale density ρ_s can be computed via the critical density ρ_{crit} at the time of the halo formation and the characteristic over-density δ_c [69].

$$\rho_s = \frac{\rho_{\text{crit}}\ \delta_c}{4} \tag{3.8}$$

The critical density for a flat universe with $\lambda = 0$ is given by [59]:

$$\rho_{\text{crit}} = \frac{3H^2}{8\pi G} \tag{3.9}$$

with the gravitational constant G and the Hubble constant [59]:

$$H = h\ 100 \frac{\text{km}}{\text{s Mpc}} \tag{3.10}$$

with $h = 0.7$. The critical density ρ_{crit} is a property of the universe and does not depend on the halo under consideration.
The characteristic over-density δ_c is given by [69]:

$$\delta_c = \frac{200}{3} \frac{c_{\text{vir}}^3}{\log(1 + c_{\text{vir}}) - \frac{c_{\text{vir}}}{1+c_{\text{vir}}}} \tag{3.11}$$

With the concentration parameter c_{vir}, a larger value implies a more compact halo, and a smaller value a more diffuse halo. The concentration parameter c_{vir} can be defined from a fit function of Concentration-Mass relation [76]:

$$\log_{10}(c_{\text{vir}}) = 1.025 - 0.097 \log_{10}\left(\frac{M_{\text{vir}}}{10^{12} h^{-1} M_\odot}\right) \tag{3.12}$$

From these fit functions, the typical corresponding concentration c_{vir} for a given virial Mass M_{vir} of the halo is obtained. This will give us then the scale density ρ_s with equation (3.8).

The fit function depends on the virial Mass M_{vir}. The halo is thought to be in gravitational equilibrium within its virial radius r_{vir}. M_{vir} is determined by assuming that the mass of the DM halo up to r_{vir} equals the mass of a sphere with the same radius but a constant density which equals 200 times the critical density ρ_{crit}:

$$M_{\text{vir}} = \frac{4\pi}{3} r_{\text{vir}}^3 \ 200 \ \rho_{\text{crit}} \tag{3.13}$$

From this equation, the corresponding virial radius r_{vir} of the halo is obtained.
Now the scale radius r_s needs to be obtained. The scale radius r_s is related to the virial radius r_{vir} and concentration c_{vir}:

$$r_s = \frac{r_{\text{vir}}}{c_{\text{vir}}} \tag{3.14}$$

By using the virial mass definition (3.13) and solving the equation after the virial radius r_{vir}, the scale radius r_s can be calculated with equation (3.14).
Then the NFW profile is defined with the two parameters r_s and ρ_s [69]:

$$\rho(r) = \frac{4\rho_s}{\frac{r}{r_s}(1+\frac{r}{r_s})^2} \tag{3.15}$$

The scale density ρ_s is also defined as the density of the NFW profile at the scale radius $\rho(r_s) = \rho_s$. In this work, the DM halos are always described with an NFW profile and therefore the halos are characterized by the two parameters ρ_s and r_s.

The process of finding ρ_s and r_s for a subhalo with a given virial Mass M_{vir} is summarized below. By inserting this virial Mass into equation (3.12), the typical concentration parameter c_{vir} for this system is obtained. This can be used to calculate the characteristic over-density δ_c from equation (3.11). Then by using equation (3.8), the scale density ρ_s is obtained.
The virial radius r_{vir} is obtained by substituting the virial mass M_{vir} into equation (3.13) and solving for r_{vir}. By using equation (3.14) with the virial concentration c_{vir} and radius r_{vir}, the scale radius r_s is obtained.

3.2.2 SpherIC

The code SpherIC is used to sample the particles and their velocities to produce a stable isolated NFW DM halo [77, 78]. Particle positions are sampled by drawing from the analytic NFW density profile, ensuring the spatial distribution matches the expected radial density. The velocities of the particles are sampled with the Eddington Inversion. This is a technique for reconstructing the velocity distribution function of a system based on its density profile [79]. This method ensures a realistic velocity distribution and produces a highly stable CDM halo, providing a robust starting point for our simulations.
For the NFW profile, the total mass would diverge and it is needed to introduce a cut-off radius r_{cutoff} to be able to apply the Eddington Inversion method. The truncated NFW density profile is defined as [78]:

$$\rho(r) = \begin{cases} \frac{\rho_0}{\frac{r}{r_s}(1+\frac{r}{r_s})^2}, & r \leq r_{\text{cutoff}}. \\ \rho(r_{\text{cutoff}})(\frac{r}{r_{\text{cutoff}}})^{\delta} e^{-\frac{r-r_{\text{cutoff}}}{r_{\text{decay}}}}, & r > r_{\text{cutoff}}. \end{cases} \tag{3.16}$$

where $\rho_0 = 4\rho_s$, and r_{cutoff} and r_{decay} are free parameters. The logarithmic slope δ is set to be continuous:

$$\delta = \frac{r_{\text{cutoff}}}{r_{\text{decay}}} - \frac{1 + 3\frac{r_{\text{cutoff}}}{r_s}}{1 + \frac{r_{\text{cutoff}}}{r_s}} \tag{3.17}$$

For all of the following simulations the free parameters of the IC are set to $r_{\text{decay}} = 0.3 r_{\text{cutoff}}$ and $r_{\text{cutoff}} = 10 r_s$.

The SpherIC code needs different parameters to generate the IC. One of the parameters is the scale radius r_s, which can be defined from the virial mass as discussed in the previous chapter 3.2.1. SpherIC also requires the mass of the halo enclosed in the outermost radius r_{outer}, which is defined by SpherIC as $r_{\text{outer}} = 100 r_s$. This Mass is calculated by integrating over the density profile. Then by defining the number of particles for the IC of the halo, SpherIC can produce the ICs.

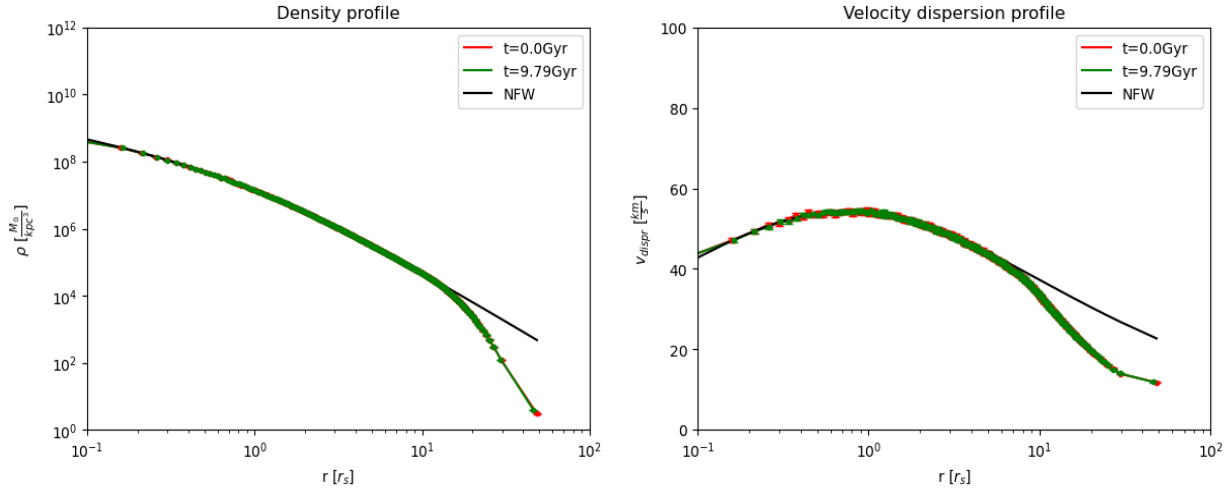

(a) (b)

Figure 9: Density (a) and velocity dispersion (b) profile of an isolated CDM halo compared to the analytic NFW density profile (black). The profile of an isolated CDM halo is shown for two time steps [$t = 0.0Gyr$ (red), $t = 9.79Gyr$ (green)]

3.3 Testing the stability of an isolated CDM halo

The IC are tested by simulating an isolated CDM halo with a virial mass of $M_{\text{vir}} = 10^{10}$. The scale density is $\rho_s = 1.4 \times 10^{-7} M_\odot \; kpc^{-3}$ and the scale radius is $r_s = 1.8$kpc. The halo is sampled for $3 * 10^6$ particles, which produces DM particles with a mass of $m_{\text{DM}} = 3170 M_\odot$. All particles have the same mass.

CDM particles interact solely through gravitational forces. As a result, the dynamics and structure of CDM halos are governed entirely by gravity. In a NFW halo, the CDM particles are distributed in a way that creates a stable equilibrium configuration. In such a halo, the particles are dynamically relaxed, meaning that over time, gravitational interactions maintain this equilibrium state without significantly altering the DM halo's structure. Therefore, it is expected to see almost no change in the structure of the CDM halo, only due to numerical inaccuracy.

In figure 9, the density and velocity dispersion profiles of the IC are compared with the analytic NFW profile. While the two profiles match closely across most of the halo, we observe a slight discrepancy in the density profile near the center of the halo. This discrepancy is expected, as resolving the innermost regions of halos in IC is challenging due to factors such as numerical resolution limits and the steepness of the central cusp. However, beyond the most inner region, the IC aligns well with the analytic NFW density and velocity dispersion profile, showing consistency up to the cut-off radius.
On the right side of figure 9, we show the evolved state of the simulation at $t = 5.2Gyr$, again compared with the analytic NFW profile. The density and velocity dispersion profiles of the halo remain almost unchanged from the IC, closely resembling the analytic profile. This stability is

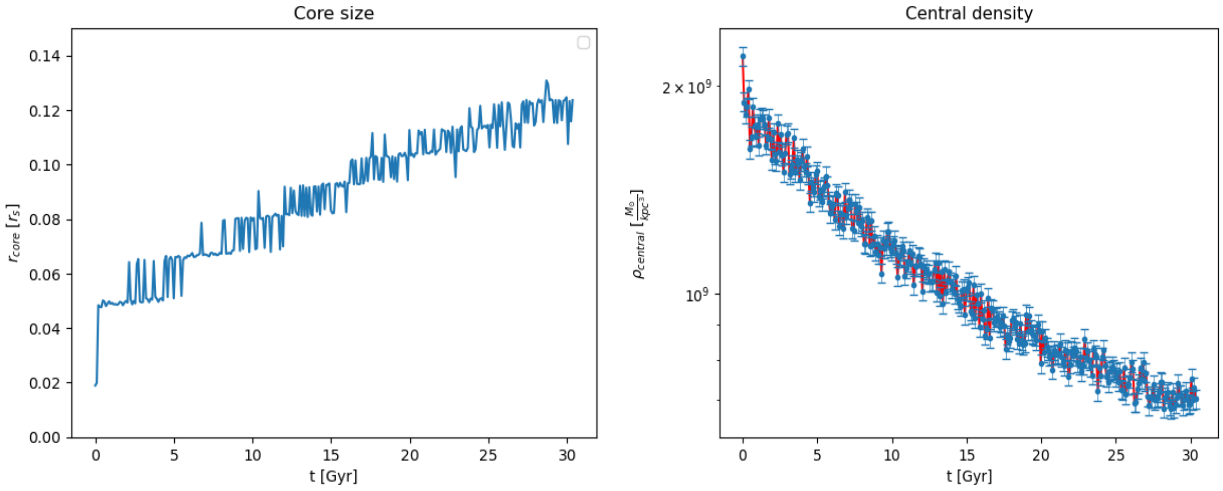

(a) (b)

Figure 10: (a) Core size evolution of an isolated CDM halo.
(b) Central density evolution of an isolated CDM halo. The central density was calculated for the 1000 innermost particles.

expected for isolated CDM halos, which should retain their NFW structure over time without significant mass redistribution. The fact that our simulation preserves the NFW profile confirms the stability of the CDM halo and the accuracy of the simulation in modeling isolated CDM systems.

On the left of figure 10, we see the core size of the simulated halo. We define the core size as the radius until the density drops to half the central density ρ_{central}. This is calculated for bins with 1000 particles. It can be seen that the core slowly increases up to 12% of the scale radius r_s. CDM halos should be stable and normally don't evolve cores as SIDM halos. Numerical inaccuracies lead to possible scattering effects between the particles through gravitational force. This is mainly observed close to the center of the DM halo. This creates a small core, which is just a numerical error.
On the right of figure 10, is the central density ρ_{central} shown for the 1000 most inner particles of the halo. It can be seen that the central density ρ_{central} initially falls and then falls increasingly slower. This means that the 1000 most inner particles spread. This also results from the numerical inaccuracies, which enable scattering effects mainly at the center.
In figure 11, the mean central density ρ_{mean} is shown. The mean central density ρ_{mean} is calculated inside two times the scale radius r_s. This figure shows that the mean central density ρ_{mean} is almost constant with small fluctuations around $9.12 * 10^6 M_\odot$. This shows the overall stability of the CDM halo.

The IC for CDM halos is overall stable. At the center of the DM halo numerical errors lead to some discrepancies. These discrepancies have no strong effect on the overall stability of the halo.

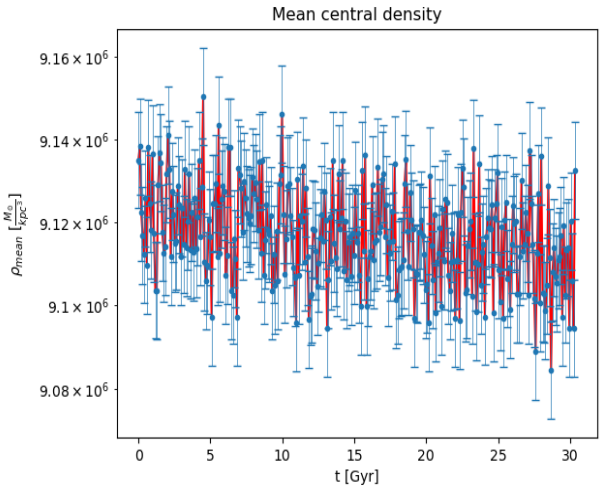

Figure 11: Mean central density evolution of an isolated CDM halo. The mean central density was calculated inside $2r_s$.

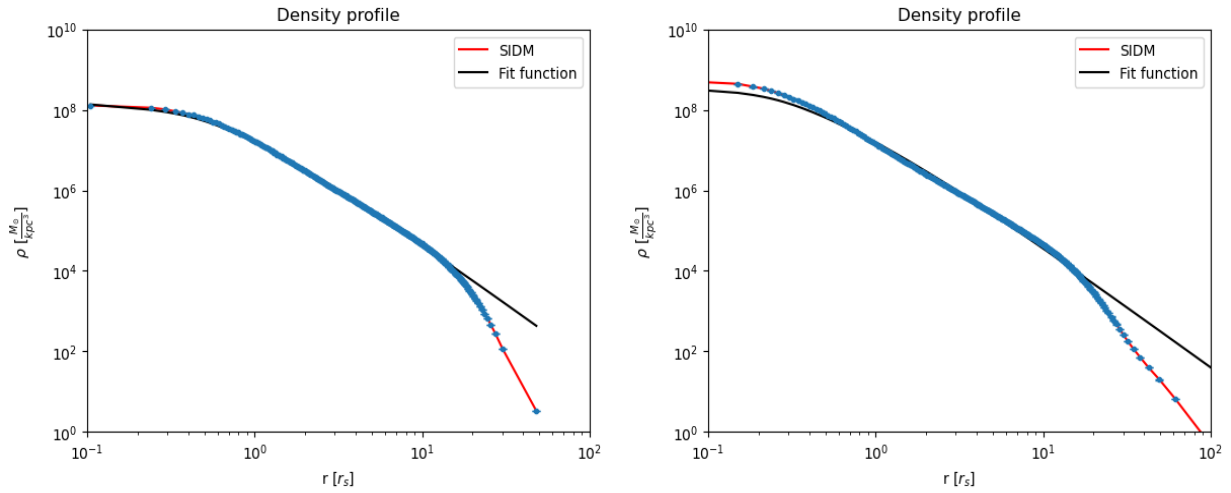

(a) $t = 1.0Gyr$ (b) $t = 3.0Gyr$

Figure 12: (a) Density profile of an isolated SIDM halo (blue) with maximum core size compared to the fit function (3.22) (black).
(b) Density profile of an isolated SIDM halo (blue) in core collapse phase compared to the fit function (3.22) (black).

3.4 Testing the evolution of an isolated SIDM halo

The already implemented framework is now tested by simulating an isolated SIDM halo. The DM particles can now scatter with each other through elastic scattering. This is simulated with the already implemented scatter routine in OpenGadget3. By default, isotropic scattering is assumed, implemented using the rSIDM scheme.

Through elastic scattering, particles within the halo exchange energy and momentum, resulting in heat transfer from the hotter regions to the colder regions. The temperature of a system is proportional to the average relative velocity, which is the velocity dispersion v_{dispr}.
In figure 9 the right panel shows the initial velocity dispersion profile. It can be seen that from the center to the scale radius r_s the velocity dispersion v_{dispr} increases (positive temperature gradient) and from the scale radius r_s to the outer region the velocity dispersion v_{dispr} decreases (negative temperature gradient). This suggests that heat transfer (energy and momentum transfer) occurs from the region around the scale radius r_s toward the central and outer regions. As the density decreases outward, the scattering probability also decreases. Therefore, the central region, up to the scale radius r_s, exchanges energy and momentum more quickly than the outer region. This produces a heat transfer from the region around the scale radius r_s toward the central region.
This heat transfer leads to the thermalization of the central halo, resulting in a constant velocity dispersion v_{dispr} in the inner region. This is shown in the left panel of figure 13. Consequently, the inner halo reaches a state of constant central density ρ_{central}, which is lower than the initial central density. This constant central density is called core. This is shown in the left panel of figure 12.
Once the central region and the area around the scale radius reach a similar temperature, an over-

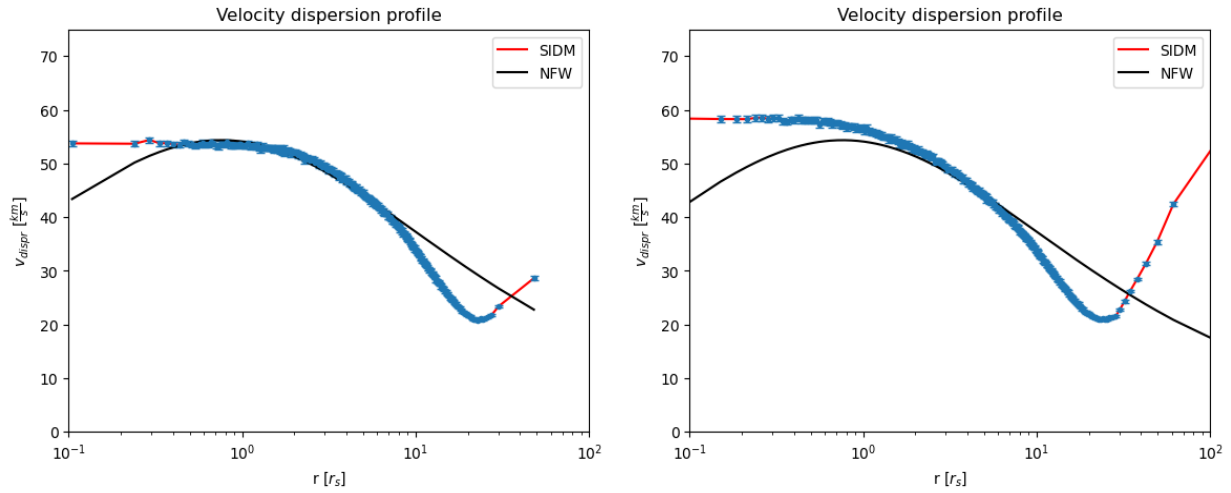

(a) $t = 1.0Gyr$ (b) $t = 3.0Gyr$

Figure 13: (a) Velocity dispersion v_{dispr} profile of an isolated SIDM halo with maximum core size (blue) compared to the NFW profile (black).
(b) Velocity dispersion v_{dispr} profile of an isolated SIDM halo in core collapse phase (blue) compared to the NFW profile (black).

all negative temperature gradient is established. Heat is gradually lost to the outer regions. This energy loss leads to the gravothermal collapse of the core, and causes the central density ρ_{central} to rise further and further above its initial value. This is shown in the left panel of figure 12. Also, the velocity dispersion v_{dispr} (temperature) keeps increasing in the inner region. This is shown in the right panel of figure 13.

The evolution of the SIDM halo is compared with a parametric model [70] to validate the already implemented framework. This model normalizes the evolution time with the collapse timescale t_c:

$$t_c = \frac{150}{C} \frac{1}{\sigma \rho_s r_s} \frac{1}{\sqrt{4\pi G \rho_s}} \tag{3.18}$$

C is a free parameter, that can be used to calibrate the parametric model. Typical values of the parameter are $C = [0.61, 0.75]$. In this thesis, the value is set to $C = 0.61$.
To confirm the evolution of the SIDM halo, the density profile and core size is compared to fit functions from the parametric model [70]. These fit functions are normalized by the collapse timescale, t_c, and describes the trajectories of key parameters: r_s (scale radius), ρ_s (scale density), and r_{core} (core radius), using a dimensionless time variable $\tilde{t} = \frac{t}{t_c}$.

$$\frac{\rho_s}{\rho_s(t=0)} = 2.033 + 0.7381\tilde{t} + 7.264\tilde{t}^5 - 12.73\tilde{t}^7 + 9.915\tilde{t}^9 - (1-2.033)(\ln 0.001)^{-1} \ln\left(\tilde{t} + 0.001\right) \tag{3.19}$$

$$\frac{r_s}{r_s(t=0)} = 0.7178 - 0.1026\tilde{t} + 0.2474\tilde{t}^2 - 0.4079\tilde{t}^3 - (1-0.7178)(\ln 0.001)^{-1} \ln\left(\tilde{t} + 0.001\right) \tag{3.20}$$

$$\frac{r_c}{r_s(t=0)} = 2.555\sqrt{\tilde{t}} - 3.632\tilde{t} + 2.131\tilde{t}^2 - 1.415\tilde{t}^3 + 0.4683\tilde{t}^4 \tag{3.21}$$

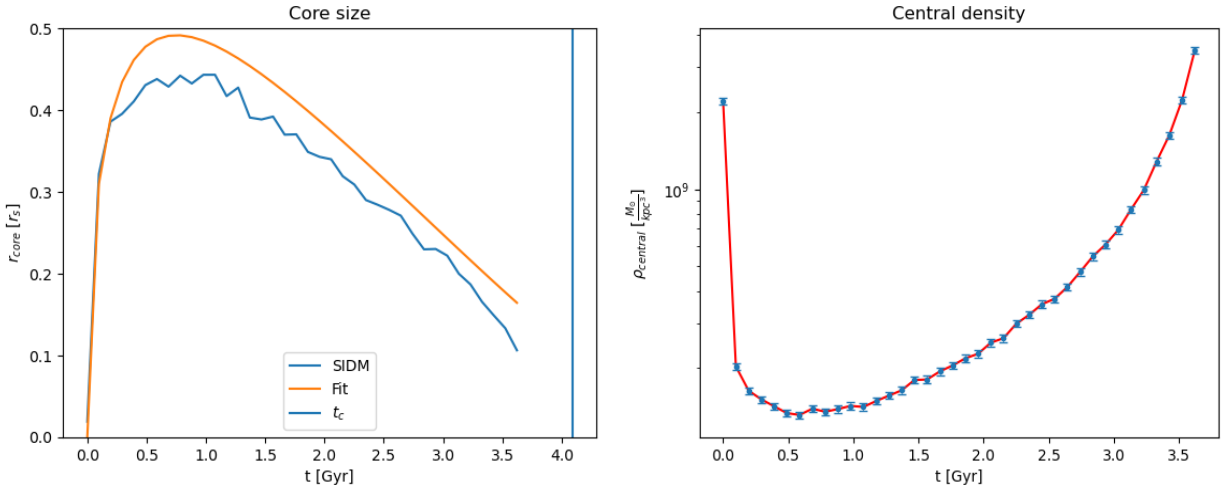

(a) (b)

Figure 14: (a) Core size r_{core} evolution of an isolated SIDM halo (blue) compared to the core size from the fit function (3.21) (orange). The blue vertical line shows the collapse timescale t_c from the equation (3.18).
(b) Central density ρ_{central} evolution of an isolated SIDM halo. The central density was calculated for the 1000 innermost particles.

The fit functions are normalized by the initial values of the key parameters and reproduce the NFW profile at $\tilde{t} = 0$.
The fit functions are then used to describe the evolution of the SIDM density profile at different times:

$$\rho_{\text{SIDM}}(r) = \frac{4\rho_s}{\frac{(r^4+r_{\text{core}}^4)^{\frac{1}{4}}}{r_s}(1+\frac{r}{r_s})^2} \tag{3.22}$$

This can be seen in the figure 12 and on the right panel of figure 15. The density profile modeled by the fit functions describes the evolution quite well. Especially when a core is formed, the analytic and simulated density profiles are very similar. For the core collapse, it can be seen that the analytic description underestimates the central density ρ_{central}, but the overall density profile and the evolution are well modeled. The velocity dispersion profile is compared to the analytic solution for the NFW profile, which serves as the IC for the simulation.

In figure 14, the evolution of the halo is detailed for the core size r_{core} and the central density ρ_{central}.
The right panel shows the central density, which initially drops quickly but then starts to slowly rise. The difference between the initial central density and the core density is about an order of magnitude. This suggests that the 1000 innermost particles initially disperse in the core expansion phase but become denser as the halo goes into core collapse.
On the left side of figure 14, the core size r_{core} of the simulated halo is shown. The core quickly grows to about half the initial scale radius r_s and then slowly contracts over time. The central den-

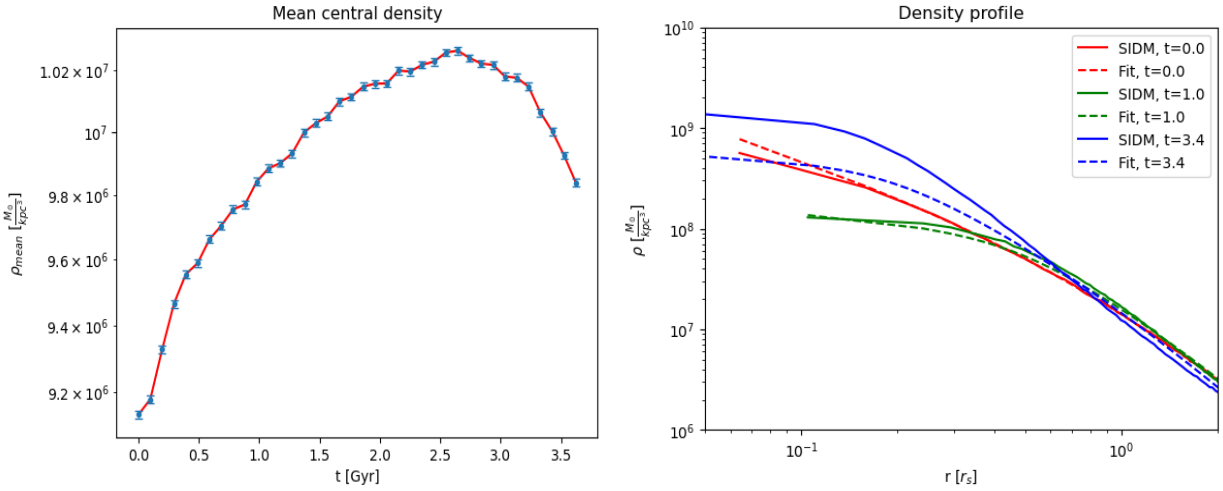

(a) (b)

Figure 15: (a) Evolution of the mean central density ρ_{mean} of an isolated SIDM halo, calculated within $2r_s$.
(b) Density profile of isolated SIDM halo (solid) at different time steps compared with fit function (dashed).

sity ρ_{central} and core size r_{core} are strongly correlated. The fit function used for core size evolution matches the overall trajectory seen in the simulation, and the collapse time is marked on the plot. The fit function successfully reproduces the general behavior of the core's evolution.
In figure 15 on the left, the mean central density ρ_{mean} illustrates how the rest of the halo responds to changes in the density and velocity dispersion during the evolution. The mean central density increases until it reaches a maximum, after which it decreases sharply.

In figure 15 on the right, the inner density profile of the SIDM halo is shown at three distinct time points. The first snapshot represents the IC. The second snapshot captures the core-expansion phase, where the core reaches its maximum size. The third snapshot is in the core collapse phase, where the halo has reached a larger central density than the initial central density. In the core collapse the difference in the central density between simulation and fit starts to increase. This can also be observed in figure 12, where the whole density profile is shown.
The fit function used for the density profile accurately captures the characteristic behavior of the halo during these different phases. The core expansion phase is very well modeled, while in the core collapse phase, especially when the central density is larger than the initial central density, the accuracy further and further decreases. This was also found in [70].
During the collapse phase, the central density continues to rise. This increase in density could potentially lead to conditions where black holes may form. As the density rises, the time steps required for the simulation become progressively smaller, increasing the computational cost significantly. Due to these constraints, further simulation is not performed beyond this phase.

4 Results

The following section shows the results from this master thesis. First, it is discussed how the different effects that are influencing the DM subhalo are modeled within OpenGadget3.
Then the DM subhalo is simulated by incorporating all these modeled effects. Simulations are conducted for both the CDM and SIDM models, with the latter tested using two different cross-sections. These simulations are used to qualitatively analyze the evolution of DM subhalos and enable a comparative study of the CDM and SIDM models.

4.1 Modeling subhalo evolution

As already discussed in chapter 2.2.4, a DM subhalo experiences external effects in a DM host halo. Those effects are the gravitational force of the DM host halo, evaporation scattering between the DM subhalo and DM host halo particles, and dynamical friction.
This thesis aims to run detailed simulations of DM subhalos but without excessive computational costs. This is achieved by resolving only the DM subhalo with N particles. The host gravitational effect is modeled with an analytic gravitational potential. Evaporation scattering between the DM particles of the host and the subhalo will be done by sampling virtual host particles. Those virtual host particles can scatter with subhalo particles through the already implemented SIDM module.

4.1.1 Analytic gravitational potential

Galaxies are constituted out of baryonic and DM structures. The most important structures to model galaxies' mass distribution are the stellar bulge, stellar disc, and the DM halo. Therefore, analytic potentials are implemented to model those three structures of the host galaxy.
The DM halo accounts for a majority of a galaxy's mass. The DM host halo is described with a NFW profile [69]. The NFW potential Φ_{NFW} is given by:

$$\Phi_{\mathrm{NFW}} = -4\pi \mathrm{G}\rho_s \frac{r_s^3}{r} \ln\left(1 + \frac{r}{r_s}\right) \tag{4.1}$$

This potential is shown in figure 4.
Stellar bulges are spheroidal or elliptical stellar structures located at the centers of galaxies. The Hernquist profile provides a suitable description of spherically symmetric stellar bulges of galaxies, especially in their dense central regions [80]. The Hernquist potential Φ_{Hern} is defined as:

$$\Phi_{\mathrm{Hern}} = -\frac{\mathrm{G}M}{r + a} \tag{4.2}$$

Stellar discs are flat, rotating structures composed of stars, gas, and dust. The Miyamoto-Nagai potential Φ_{Disc} describes those stellar discs and can be used to describe thin and thick discs [81]:

$$\Phi_{\mathrm{Disc}} = -\frac{\mathrm{G}M}{\sqrt{(a^2 + \sqrt{b^2 + z^2})^2 + x^2 + y^2}} \tag{4.3}$$

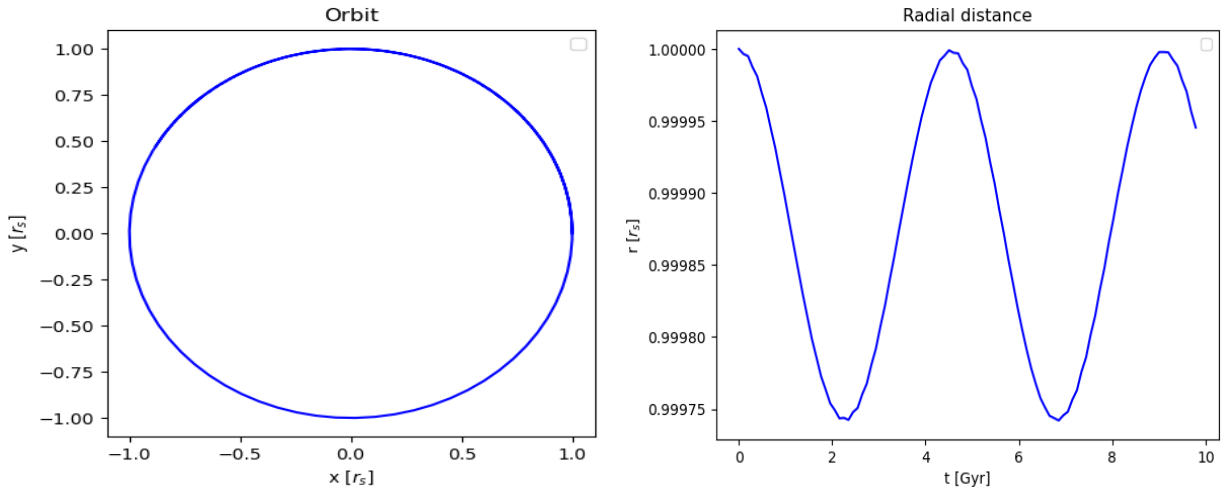

(a) (b)

Figure 16: (a) Circular orbit of a test particle in an NFW gravitational potential, plotted in the x-y plane.
(b) Radial distance of the test particle as it maintains a circular orbit.

By combining these three potentials – the NFW potential for the DM host halo, the Hernquist potential for its stellar bulge, and the disc potential for the stellar disc – we can comprehensively model both the dark matter and stellar components of the host galaxy system.

The acceleration acting on a particle is derived from the gradient of the gravitational potential. In OpenGadget3, this acceleration is implemented using the following formulation:

$$a^i_{\mathrm{NFW}} = 4\pi G\rho_s \frac{r_s^3}{r^3}\left(\frac{r}{r+r_s} - \ln\left(\frac{r+r_s}{r}\right)\right) * dx^i \tag{4.4}$$

$$a^i_{\mathrm{Hern}} = -\frac{\mathrm{G}M}{r(r+a)^2} * dx^i \tag{4.5}$$

This is done for the spatial coordinates (i=1,2,3). For the disc potential, the acceleration in the z-direction (i=3) is differently defined than for the other two spatial directions.

$$\begin{aligned} a^i_{\mathrm{Disc}} &= -\frac{\mathrm{G}M}{((a+\sqrt{b^2+z^2})^2 + x^2 + y^2)^{\frac{3}{2}})} * dx^i \\ a^z_{\mathrm{Disc}} &= -\frac{\mathrm{G}M}{((a+\sqrt{b^2+z^2})^2 + x^2 + y^2)^{\frac{3}{2}})} \frac{a+\sqrt{b^2+z^2}}{\sqrt{b^2+z^2}} * dz \end{aligned} \tag{4.6}$$

Those accelerations are then added to the total acceleration of each particle.

This thesis focuses only on the DM halo of the satellite and the host galaxy.
To validate the analytic NFW potential, it is tested with a single test particle. First, the theoretical circular velocity v_{circ} is calculated for a given radius r. Using these as IC $[v_{\mathrm{circ}}, r]$, the motion of the

test particle is simulated. As shown in figure 16, the test particle moves along a circular orbit. The right panel shows only very small fluctuations around the circular orbit, confirming the accuracy of the implementation.
In figure 21, the blue line represents a simulation of a DM subhalo on a circular orbit without evaporation effects. Unlike the test particle, the DM subhalo, due to its extended structure, follows an almost circular orbit rather than a perfectly circular one.

4.1.2 Evaporation

Currently, the particles within the DM subhalo can only scatter among themselves. In a more realistic scenario, the host halo would be resolved with particles, allowing for scattering interactions between the subhalo and the host halo particles. These interactions would result in a loss of particles from the subhalo and decelerate the subhalo, a phenomenon known as evaporation.
To account for the evaporation effect without explicitly resolving the host halo with particles, virtual host particles are introduced. For every DM particle in the subhalo, a number of virtual DM host halo particles (denoted as N_{ngb}) are generated. Those virtual host particles are sampled at the same location as the DM subhalo particle. The already implemented SIDM module simulates scattering between the DM subhalo and their virtual DM host halo particles.

Implementation into OpenGadget3 For each time step, the simulation first processes the scattering between DM subhalo particles, and then the evaporation scattering between DM subhalo particles and virtual DM host halo particles.
For each DM subhalo particle, the virtual particles are sampled and used for scattering calculations with the SIDM module. After scattering, these virtual particles are discarded and re-sampled in the next time step. This approach allows us to simulate the evaporation effect, maintaining computational efficiency while introducing realistic scattering interactions between the DM subhalo and the DM host halo.
To simulate evaporation scattering with the SIDM module, it is necessary to calculate the smoothing length h based on the following equation:

$$h^3 = \Lambda m \frac{N_{\mathrm{ngb}}}{\rho(r)} \tag{4.7}$$

m is the mass of the virtual particles, which is assumed to be equal to the mass of the subhalo particles. N_{ngb} is the number of virtual host halo particles sampled for each subhalo particle. $\rho(r)$ is the density of the host halo at the location of the subhalo particle, for which we sample the virtual particles. Λ represents the kernel overlap, which is already implemented as a function in OpenGadget3 [72].
When simulating the evaporation effect, various outcomes can occur during the scattering between DM subhalo and DM host halo particles. These scenarios are:

1) Both particles are unbound to the subhalo after scattering
2) Both particles are bound to the subhalo after scattering
3) The subhalo particle remains bound, while the host halo particle remains unbound to the subhalo.
4) The subhalo particle becomes unbound, while the host halo particle becomes bound.

The first scenario is already handled by the current simulation setup. The DM subhalo particle continues to be simulated and the virtual DM host halo particle is discarded.
The second scenario has not yet been implemented. To model this case, it is necessary to convert the virtual particle into a DM subhalo particle instead of discarding it after the interaction.
The third scenario is already covered by the existing setup of the simulation. The subhalo particle

continues to be simulated and the virtual host halo particle is discarded.
For the fourth scenario OpenGadget3 already has an implementation, as referenced in [48]. When the scattering angle between the subhalo and virtual host halo particle exceeds 90°, the host halo particle becomes most likely bound, and the subhalo particle becomes most likely unbound. To handle this, the simulation switches the scatter angles of the two particles (mimics switching labels): the virtual host halo particle is labeled as a subhalo particle, and the original subhalo particle is labeled as a virtual host halo particle and gets discarded. This implementation is called SANGLE in OpenGadget3.

Deceleration Problem The first test for implementing the evaporation effect is the deceleration problem [47]. In this test, a single test particle moves through a background with a constant density ρ. The background particles are at rest. The test particle is decelerated by these background particles.
The background particles are represented by the virtual particles. Those are sampled at the radius of the test particle by the implemented evaporation scheme. The evaporation scheme simulates the scattering between the virtual and test particles. Then the virtual particles are discarded.
In this scenario, we use the fSIDM module to simulate the scattering. In fSIDM, the scattering cross-sections are such that the typical scattering angles are very small, leading to an effective drag force. This means that particles experience deceleration due to interactions with the surrounding matter, but the direction of movement does not change significantly.
We chose this scenario with fSIDM because we can effectively test our implementation against a

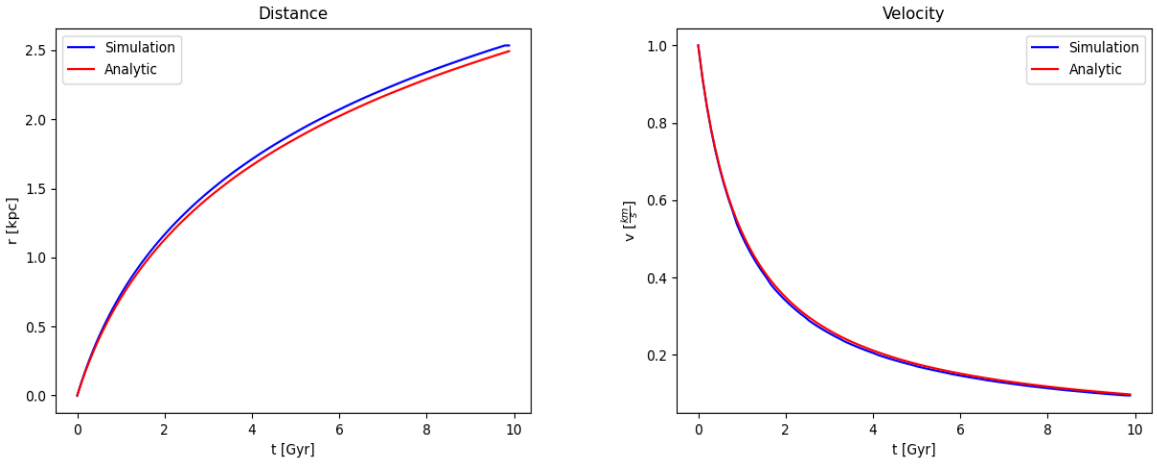

(a) (b)

Figure 17: (a) Distance of a test particle from it's initial position as it moves through a constant background density ρ, compared between the simulated trajectory (blue) and the analytic prediction from equation (4.8) (red).
(b) Velocity of the test particle compared between the simulation (blue) and the analytic solution from equation (4.8) (red).

simple analytic expression. Since the scattering angles are small, the test particle slows down but retains its general direction. The analytic trajectory of the test particle, subject to the drag force, can be derived from the following equation [47]:

$$\ddot{x} = -\frac{1}{2}\dot{x}^2 \rho \frac{\sigma_{\tilde{T}}}{m_\chi} \tag{4.8}$$

The test simulation is done for a background density of $\rho = 4.46 * 10^7\ M_\odot\ \mathrm{kpc}^{-3}$. The self-interaction cross-section is $\frac{\sigma_{\tilde{T}}}{m_\chi} = 200\frac{\mathrm{cm}^2}{\mathrm{g}}$. For each time step $N_{\mathrm{ngb}} = 64$ particles of the background are sampled at the coordinates of the test particle and then potential scatter is calculated.
Figure 17 shows the analytic and simulated solutions, which closely match, confirming that our evaporation implementation aligns well with the expected results.

Expected number of scatter events For the second test for implementing the evaporation effect, we simulate a DM halo moving v through a constant background density ρ. The background particles are at rest and are represented by the virtual particles. The evaporation scheme simulates the scattering between the virtual and test particles. For this test, the rSIDM module is used with an isotropic cross-section to simulate the scattering.
This setup has an analytic description for the probability of scatter events for one halo particle [47]:

$$P = \frac{\sigma_{\tilde{T}}}{m_\chi} v \rho \tag{4.9}$$

The probability depends on the density of the background ρ, the velocity of the halo v, and the cross-section $\frac{\sigma_{\tilde{T}}}{m_\chi}$. The actual velocity for the scattering between particles varies from the velocity of the halo v, because of the velocity dispersion inside the halo. A much larger halo velocity v as the velocity dispersion reduces the error arising from that assumption.
By multiplying the probability P with the total number of halo particles N and the size of the timestep Δt, we get the expected number of scatter events n in a given timestep:

$$n = NP\Delta t \tag{4.10}$$

The test simulation is done for a background density of $\rho = 2.46 * 10^4\ M_\odot\ \mathrm{kpc}^{-3}$. The self-interaction cross-section is $\frac{\sigma_{\tilde{T}}}{m_\chi} = 50\frac{\mathrm{cm}^2}{\mathrm{g}}$ and the halo has initial a velocity of $v = 343.15\frac{km}{s}$. For each time step $N_{\mathrm{ngb}} = 48$ particles of the background are sampled at the coordinates of each DM halo particle and then potential scatter is calculated.
In figure 18, the analytic and simulated number of scatter events are shown and they closely match (a relative error of a few percent), confirming that our evaporation implementation aligns well with the expected results.
The error starts to rise at the end. This occurs as the halo slows down due to the evaporation scattering. The momentum and kinetic energy exchange between the halo particles and the background particles causes the halo to decelerate. The reduced velocity decreases the scatter probability. As the halo's velocity is not updated for the probability of scatter events, this induces an increasing error over time.

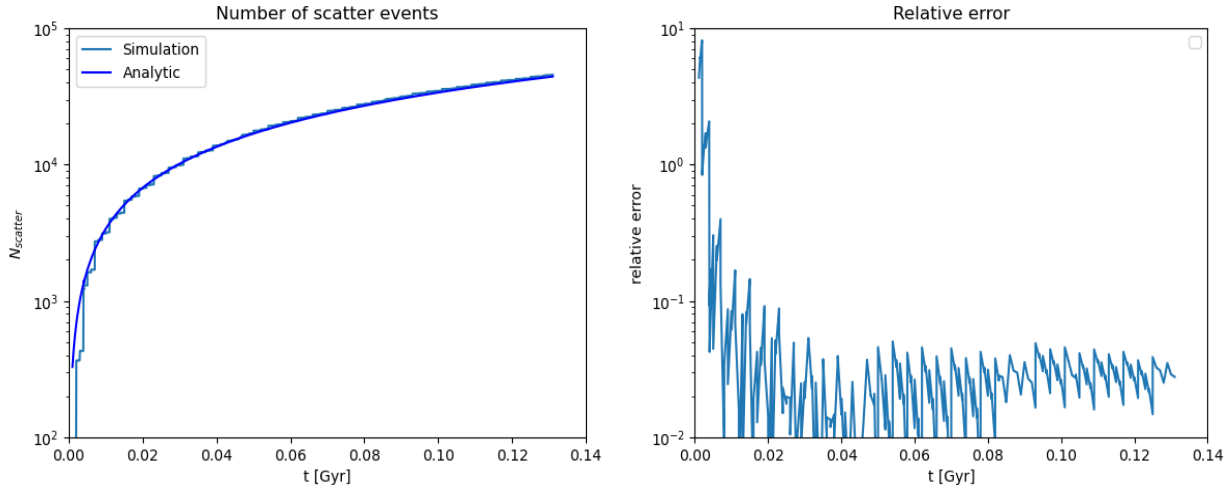

(a) (b)

Figure 18: (a) Number of scatter events N_{scatter} caused by evaporation between a SIDM halo and a constant DM background density ρ, compared between the simulation results (light blue) and the analytic prediction from equation (4.10) (dark blue).
(b) The relative error between the simulation and the analytic prediction is shown.

Eddington Inversion Now an evaporation scattering routine is implemented using virtual host particles. So far, those virtual host particles were only at rest. The virtual host particles should represent the local environment of the DM host halo to realistically model evaporation scattering. Therefore, they should have typical velocities for the local host system. As discussed earlier in chapter 3.2.2 sampling the velocities with the Eddington Inversion produces a realistic and stable NFW halo. The resulting particles realistically represent the local environment of the host halo.
We want to use the Eddington Inversion to sample particles that are bound to the host system [68, 79]. The relative energy per unit mass ϵ is defined as:

$$\epsilon = \frac{v^2}{2} + V(r) \tag{4.11}$$

where $V(r)$ is the relative gravitational potential per unit mass. A particle is considered to be bound if $\epsilon \leq 0$.

We implemented the Eddington Inversion as in the SpherIC code [77, 78]. The simplest case is considered, which is a spherically symmetric and isotropic distribution. In that case the distribution function $f = f(\epsilon)$ only depends on the relative energy ϵ and not on the relative angular momentum. For this case the density profile $\rho(r)$ is connected to the distribution function $f(\epsilon)$ by the equation [68, 79]:

$$\rho(r) = \int_0^\infty d\vec{v} f(\epsilon) = 4\pi \int_0^{v_{\max}(r)} dv v^2 f(\epsilon) \tag{4.12}$$

As we consider a system of bound particles, the maximum velocity $v_{\max}(r)$ a particle can have and is still bound, is defined for $\epsilon = 0 = \frac{v_{\max}^2(r)}{2} + V(r)$. This can be used as the upper integral limit.

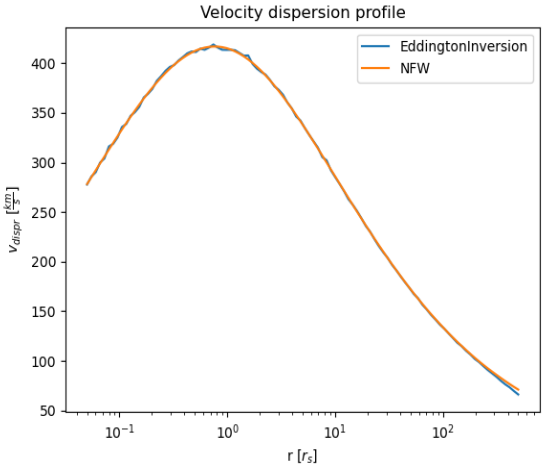

Figure 19: Comparison between the produced velocity dispersion via the Eddington Inversion (blue) and the analytic NFW velocity dispersion (orange).

Solving the equation (4.11) for the velocity v and then deriving with respect to the relative energy per unit mass ϵ gives $dv = \frac{d\epsilon}{\sqrt{2(\epsilon - V(r))}}$. By inserting v and dv into the equation (4.12), the resulting equation for the density profile is then:

$$\rho(r) = 4\pi\sqrt{2}\int_0^{V(r)} f(\epsilon)\sqrt{\epsilon - V(r)}d\epsilon \tag{4.13}$$

The upper limit comes from $v = 0$, which results in $\epsilon = V(r)$ from equation (4.11) and the lower limit from the maximum velocity $v_{\max}(r)$, which results in $\epsilon = 0$.
The relative gravitational potential V is a monotonic function of the radius r, so the variables can be changed from r to V. Therefore, the equation (4.13) can be differentiated with respect to $V(r)$:

$$\frac{d\rho}{dV} = \sqrt{8}\pi\int_0^{V} \frac{f(\epsilon)}{\sqrt{\epsilon - V}}d\epsilon \tag{4.14}$$

By inverting this equation with the Abel transform inversion formula, we get the Eddington formula [68, 79]:

$$f(\epsilon) = \frac{1}{\sqrt{8}\pi^2}\frac{d}{d\epsilon}\int_0^{\epsilon}\frac{dV}{\sqrt{V-\epsilon}}\frac{d\rho}{dV} \tag{4.15}$$

Now this equation can be simplified by integrating by parts, which gives the equation:

$$f(\epsilon) = \frac{1}{\sqrt{8}\pi^2}\frac{d}{d\epsilon}\left(\left[\sqrt{V-\epsilon}\frac{d\rho}{dV}\right]_0^{\epsilon} - \int_0^{\epsilon} 2\sqrt{V-\epsilon}\frac{d^2\rho}{dV^2}dV\right) = \frac{1}{\sqrt{8}\pi^2}\int_0^{\epsilon}\frac{dV}{\sqrt{V-\epsilon}}\frac{d^2\rho}{dV^2} \tag{4.16}$$

By defining $\sqrt{\frac{V}{\epsilon}} = \sin(x)$, this equation can be further simplified to:

$$f(\epsilon) = \frac{\sqrt{-\epsilon}}{\sqrt{2}\pi^2}\int_0^{\frac{\pi}{2}}\sin(x)\frac{d^2\rho}{dV^2}dx \tag{4.17}$$

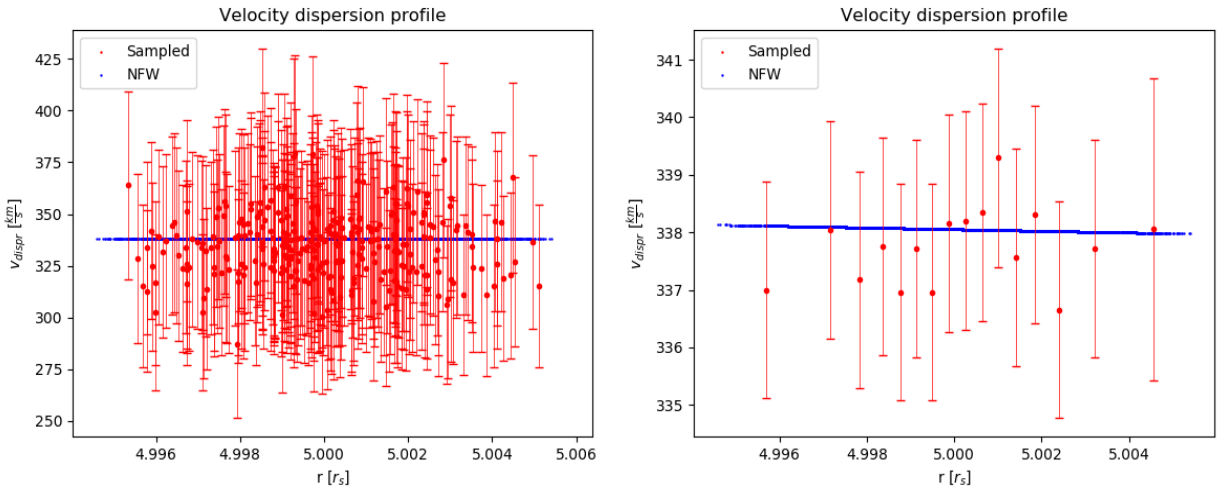

(a) (b)

Figure 20: (a) Velocity dispersion of sampled virtual host particles at the radii of each subhalo particle (red) compared to the analytic NFW velocity dispersion (blue).
(b) Velocity dispersion using combined bins of sampled virtual host particles (red) compared to the analytic NFW velocity dispersion (blue).

This equation is then solved numerically with the trapezoidal rule. Then for sampling the velocities, the acceptance-rejection technique for Monte Carlo sampling is used. This sampling procedure is done from the distribution function (4.17) [77, 78].

The accuracy of our implemented sampling method is first tested by reproducing a full velocity dispersion profile.
For this test, particles are sampled within the range of $0.05r_s$ to $500r_s$ across 100 logarithmically spaced radii. At each radius, $1e4$ particles were sampled and their velocity dispersion was calculated.
In figure 19 sampled velocity dispersion profile is compared to the analytic profile. We see that the sampling routine reproduces the velocity dispersion profile very well. There is only a significant difference at large radii.

Now the sampling method is tested within the scattering routine. We start a simulation of a DM subhalo with the implemented evaporation scheme. This DM subhalo is on a circular orbit at 5 times the scale radius r_s of the host. We collect the velocities and the radius of the virtual host particles that are sampled due to the scattering routine.
In figure 20 the velocity dispersion of the virtual host particles is compared to the analytic velocity dispersion. For this test, 64 virtual host particles were sampled for each DM subhalo particle. The velocity dispersion is only compared at radii where the DM subhalo particles are located.
It can be seen that the sampling routine reproduces the velocity dispersion profile very well. If several bins are combined to increase the accuracy, the error bars are getting much smaller and still reproduce the velocity dispersion profile very well. This can be seen on the right side.

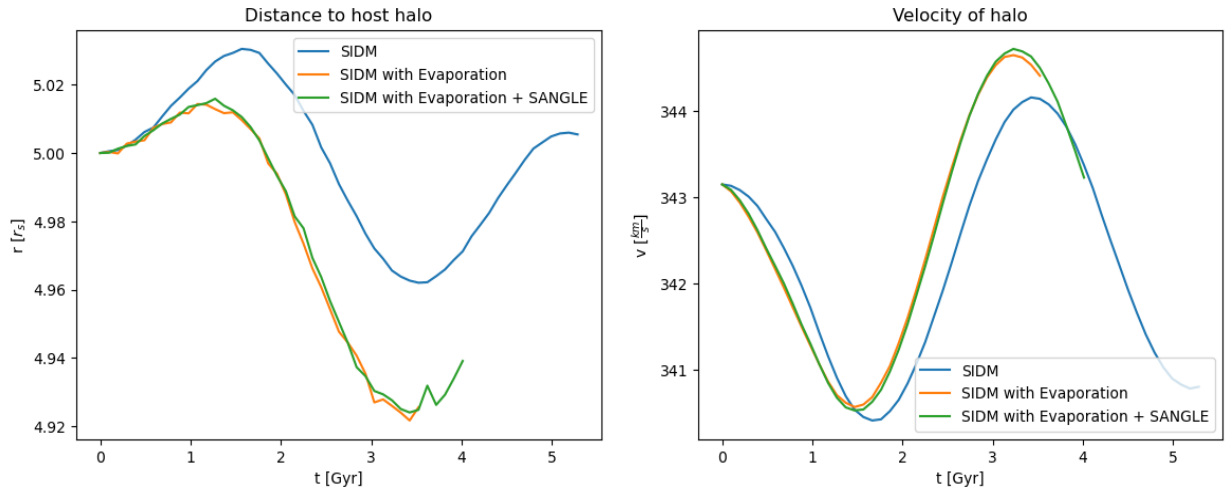

(a) (b)

Figure 21: (a) The radial distance of subhalos from the host center for an initial circular orbit, simulated for a SIDM subhalo without evaporation (blue), with evaporation (orange) and with evaporation and SANGLE (green).
(b) The velocity of the same subhalos: without evaporation (blue), with evaporation (orange) and with evaporation and SANGLE (green).

SIDM subhalo on circular orbit Now the evaporation scattering is investigated, how it affects the evolution of a SIDM subhalo. Therefore, a SIDM subhalo with and without the evaporation scheme is simulated.
The SIDM subhalo was initialized on a circular orbit around its DM host halo. The DM host halo is described by the analytic NFW potential. To understand the impact of evaporation scattering, three versions of the simulation are run: one without evaporation scattering and two with evaporation scattering (one with and the other without SANGLE). In all cases, a constant cross-section of $50\text{cm}^2/\text{g}$ is assumed for the self-interactions.

The host system has a virial mass of $10^{13}M_\odot$, a concentration of $c_{\text{vir}} = 8.77$, a scale radius of $r_s = 50.67\text{kpc}$, and a scale density of $\rho_s = 1.10668 \times 10^{-4}M_\odot/\text{kpc}^3$. The subhalo has a virial mass of $10^{10}M_\odot$, a concentration of $c_{\text{vir}} = 17$, a scale radius of $r_s = 2.59\text{kpc}$, and a scale density of $\rho_s = 2.37445 \times 10^{-3}M_\odot/\text{kpc}^3$. The subhalo is initially positioned at five times the host's scale radius $5r_s$ and given the circular velocity corresponding to that radius, approximately $343\frac{\text{km}}{\text{s}}$.

In figure 21 the orbital parameters of the simulated SIDM subhalos are shown. In the simulation without evaporation (blue curve), the SIDM subhalo maintained an almost circular orbit. The simulations with evaporation (green and orange curve) show a faster decline of the radius. This effect is due to the continuous exchange of momentum and kinetic energy between the DM subhalo and DM host particles. This reduces the momentum and kinetic energy of the subhalo, which effectively reduces the velocity of the subhalo. This gradual loss of orbital energy causes the subhalo to spiral toward the host's center. This process is known as orbital decay.

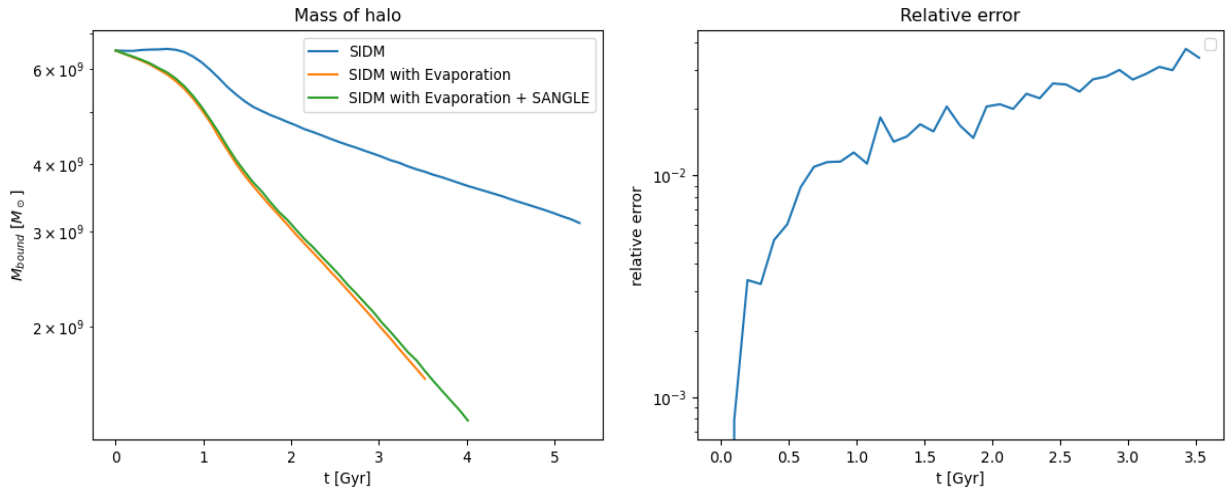

(a) (b)

Figure 22: (a) The bound mass M_{bound} of subhalos on an initial circular orbit. The SIDM subhalos are simulated without evaporation (blue), with evaporation (orange) and with evaporation and SANGLE (green).
(b) The relative error between the simulations with evaporation, comparing cases with and without SANGLE.

On the left side in figure 22, the bound mass M_{bound} of the SIDM subhalo is shown. It can be seen that the SIDM subhalo with evaporation loses significantly more mass. At the beginning of the simulation, the difference in the bound mass arises mostly from the evaporation scattering. This evaporation scattering occurs due to the high central density mostly in the inner region. SIDM subhalo particles are typically accelerated to higher velocities due to evaporation scatterings. If those velocities reach or exceed the local escape velocity $v \geq v_{\text{esc}}(r)$, the particles can become unbound and reduce the bound mass of the SIDM subhalo.
This leads to a reduction of the central density. A reduction of the central density leads to a less deep gravitational potential. A less deep gravitational potential can not hold the high-velocity particles in the central region. Therefore the central velocity dispersion decreases.
This has a profound impact on the core dynamics of SIDM halos. For a core collapse to occur, there needs to be a flow of energy from the inner core to the outer regions. This is only possible if the central velocity dispersion is higher than that of the outer regions. However, evaporation scattering prevents this energy flow by continuously lowering the core's velocity dispersion. As a result, instead of collapsing, the core expands as kinetic energy is further transferred inward from the outer regions.
A core has a lower central density compared to the initial NFW profile. This lower central density results in a shallower gravitational potential for the SIDM subhalo. This is connected to less strongly bound DM subhalo particles. Therefore, tidal forces can strip particles more efficiently. In figure 22 the SIDM subhalo without evaporation (blue curve) only experiences a significant loss of mass when the SIDM subhalo has reached its maximum core size. As the core size r_{core} decreases,

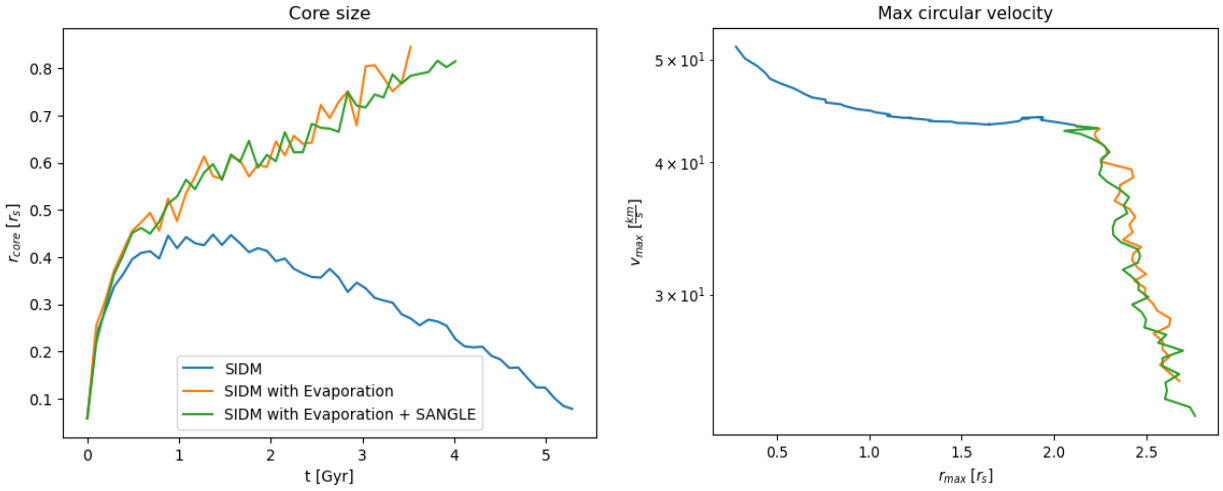

(a) (b)

Figure 23: (a) The core size r_{core} of the subhalos on an initial circular orbit, simulated without evaporation (blue), with evaporation (orange) and with evaporation and SANGLE (green).
(b) The maximum circular velocity v_{max} and the corresponding radius r_{max} of the subhalos: without evaporation (blue), with evaporation (orange) and with evaporation and SANGLE (green).

the SIDM subhalo experiences less mass loss. For the simulations with evaporation the core always continues to increase. This continuous core expansion made the SIDM subhalo more susceptible to further mass loss.

As discussed in chapter 4.1.2, there are different scenarios for the evaporation scattering. One additional scenario is already implemented and is called SANGLE. This scenario introduces a relative error in the bound mass M_{bound} on the order of $\mathcal{O}(10^{-2})$ (shown in figure 22 on the right panel), indicating that it had a minor influence on the system's evolution. The core size evolves the same with and without the SANGLE implementation.

The maximum circular velocity v_{max} and its corresponding radius are key observables of the DM halos (shown in figure 23 on the right panel). They are connected to the enclosed mass via the equation (2.1). In the simulation without evaporation, the maximum circular velocity remains almost constant for a long time but shifts closer to the center. As the halo undergoes core collapse, v_{max} increases and still shifts closer to the center. In contrast, the simulation with evaporation results in a strong decline in maximum circular velocity, which also shifts slightly outward. The strong decline results from the large loss of bound mass.

The evolution of the density maps of the SIDM subhalos (figure 24) reveals differences between the two simulations (with and without evaporation). Initially, the DM subhalo is a spherically symmetric structure. As the simulation progresses, tidal forces from the host halo caused the subhalo to elongate radially $t = 0.4$Gyr. Stripped particles form tidal streams that trail behind and lead ahead of the subhalo along its orbit $t = 2.0$Gyr. This change of structure is very similar in both simulations, but a key distinction is easy to see: in the presence of evaporation scattering, a diffuse

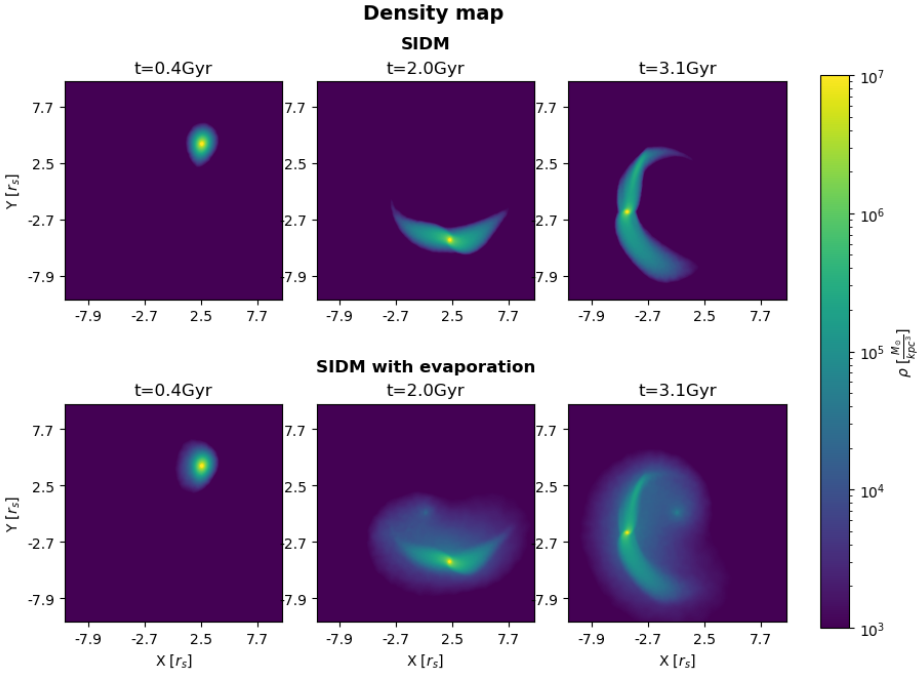

Figure 24: The density maps of the simulated SIDM subhalos without evaporation (top) and with evaporation and SANGLE (bottom) is shown for three different time steps in the x-y plane.

cloud of low density formed around the SIDM subhalo. This cloud was the result of evaporation scattering, where particles were scattered out of the DM subhalo into the surrounding host system. Additionally, in the simulation with evaporation, a minor density peak emerged at the center of the DM host halo, suggesting that some of the scattered DM particles were being redistributed into the host's central regions $t = 3.1$Gyr.

As discussed in chapter 2.2.3, a velocity-dependent cross-section could address the issues faced at small scales while preserving the successes of CDM on larger scales. The current simulations demonstrate that evaporation scattering suppresses the core collapse phase when a constant cross-section is used. A velocity-dependent cross-section can reduce the impact of evaporation scattering while maintaining the effectively same self-interaction rate within the SIDM subhalo. This would allow SIDM subhalos to experience both core expansion and collapse phases with evaporation, while aligning with observational constraints.

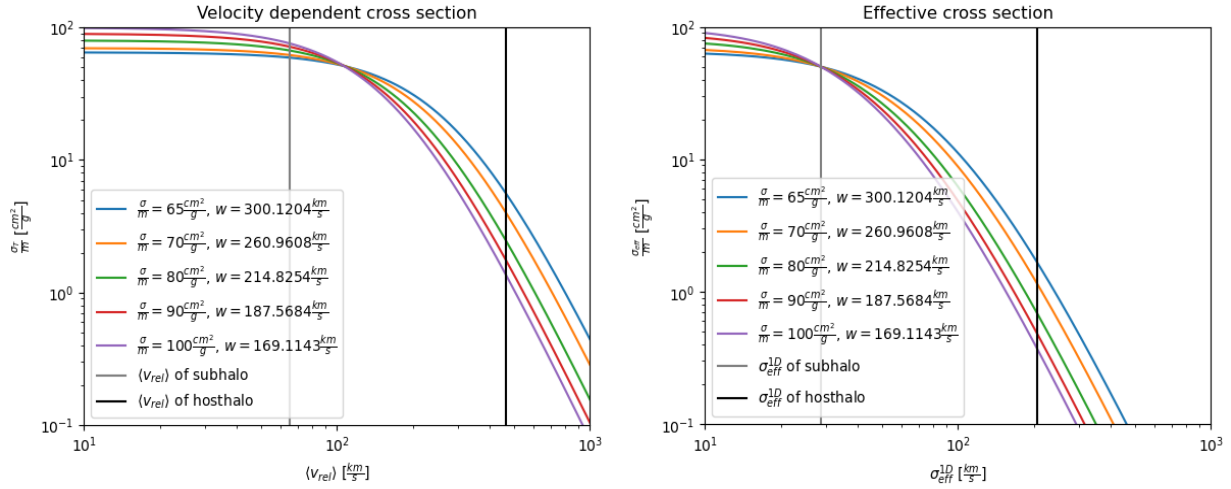

(a) (b)

Figure 25: (a) The velocity dependent cross section $\frac{\sigma_T}{m}$ from equation (4.18) as a function of the scattering velocity v_{scatter}. This is shown for 5 different values of $\frac{\sigma}{m}$ and w. The average relative velocity $\langle v_{\text{rel}} \rangle$ of the subhalo (grey) and hosthalo (black) are plotted as vertical lines.
(b) The effective cross section $\frac{\sigma_{\text{eff}}}{m}$ from equation (4.23) as a function of the characteristic velocity dispersion $\sigma_{\text{eff}}^{\text{1D}}$. The characteristic velocity dispersion of the subhalo (grey) and hosthalo (black) are plotted as vertical lines.

4.2 Velocity-dependent cross-section

So far, a constant velocity-independent cross-section $\frac{\sigma_{\text{const}}}{m} = 50\frac{\text{cm}^2}{\text{g}}$ has been applied. From now on, a velocity-dependent cross-section will be used. The velocity-dependent cross-section should be designed to replicate the SIDM subhalo core evolution observed with the constant cross-section while reducing the likelihood of evaporation events.
The velocity-dependent cross-section is typically modeled with a momentum transfer cross-section as [72]:

$$\frac{\sigma_T}{m} = \frac{\frac{\sigma}{m}}{(1 + (\frac{v}{w})^2)^2} \tag{4.18}$$

The effective cross-section for a system is given by [72]:

$$\frac{\sigma_{\text{eff}}}{m} = \frac{\langle v_{\text{rel}}^5 \frac{\sigma_T}{m} \rangle}{\langle v_{\text{rel}}^5 \rangle} \tag{4.19}$$

and depends on the relative velocities v_{rel} of a given system. The effective cross-section for the subhalo should be the same as the constant to replicate the SIDM subhalo core evolution.
Therefore, the typical relative velocity $\langle v_{\text{rel}} \rangle$ of a DM subhalo is needed to know. The distribution of the relative velocities for a DM halo can be described by [82]:

$$f(v_{\text{rel}}) = \frac{1}{\sqrt{4\pi}} \frac{v_{\text{rel}}^2}{(\sigma_{\text{eff}}^{\text{1D}})^3} \exp\left\{ (-\frac{v_{\text{rel}}^2}{4(\sigma_{\text{eff}}^{\text{1D}})^2}) \right\} \tag{4.20}$$

This distribution depends on the characteristic velocity dispersion $\sigma_{\text{eff}}^{\text{1D}}$ of a DM halo. This characteristic velocity dispersion can be approximated with the maximal circular velocity v_{max} of this halo [83]:

$$\sigma_{\text{eff}}^{\text{1D}} = \frac{v_{\text{max}}}{\sqrt{3}} \tag{4.21}$$

The maximal circular velocity is computed from the initial density profile, which is the NFW profile. By integrating the density profile, the enclosed mass profile is obtained and from equation (2.1), the maximum value and the corresponding radius can be found.
The average relative velocity $\langle v_{\text{rel}} \rangle$ of a halo is defined as

$$\langle v_{\text{rel}} \rangle = \int_0^\infty v_{\text{rel}} f(v_{\text{rel}}) dv_{\text{rel}} = \frac{4 v_{\text{max}}}{\sqrt{3\pi}} \tag{4.22}$$

and can be expressed with the characteristic velocity dispersion v_{max}.
By inserting the velocity-dependent cross-section and the distribution of the relative velocities of a halo into the effective cross-section, the equation yields:

$$\sigma_{\text{eff}} = \frac{\sigma}{768(\sigma_{\text{eff}}^{\text{1D}})^8} \int_0^\infty \frac{v_{\text{rel}}^7}{(1 + (\frac{v_{\text{rel}}}{w})^2)^2} \exp\left(-\frac{v_{\text{rel}}^2}{4(\sigma_{\text{eff}}^{\text{1D}})^2}\right) dv_{\text{rel}} \tag{4.23}$$

By solving this equation for the characteristic velocity dispersion $\sigma_{\text{eff}}^{\text{1D}}$ of the host, we get the effective cross-section for the host system. For the characteristic velocity dispersion $\sigma_{\text{eff}}^{\text{1D}}$ of the DM subhalo, we get the effective cross-section for the subhalo, which relates to how quickly the DM subhalo evolves. The subhalo should evolve as the DM subhalo with the constant cross-section. Therefore, the effective cross-section of the DM subhalo is set to be the same as the constant cross-section $50\frac{cm^2}{g}$. The effective cross-section for the host system is chosen to be in the order of $\mathcal{O}(0.1 - 1\frac{cm^2}{g})$. This provides a corresponding range of values for $\frac{\sigma}{m}$ and w, tailored to match the expected velocity scales of the DM host and subhalo.
In figure 25 possible velocity-dependent cross-sections are shown with their corresponding effective cross-sections. On the left side, the different velocity-dependent cross-sections are shown as a function of relative velocities for the scattering. Average relative velocities of the sub and host halo are shown.
On the right side, the effective cross-section is shown as a function of characteristic velocity dispersion. The characteristic velocity dispersion is shown for the DM host and subhalo. It can be seen that the effective cross-sections reach $50\frac{\text{cm}^2}{\text{g}}$ for the characteristic velocity dispersion of the DM subhalo. The effective cross-section of the DM host halo is slightly above zero. Thus, reducing the interaction rate for the DM host halo and evaporation scattering.

To confirm that the DM subhalo evolves the same for the velocity-dependent cross-section as for the constant cross-section, an isolated DM subhalo is simulated once with a constant cross-section and once with the corresponding velocity-dependent cross-section. This is done for two different constant cross-sections $[10\frac{\text{cm}^2}{\text{g}}, 50\frac{\text{cm}^2}{\text{g}}]$ and their corresponding velocity-dependent cross-section. Those velocity dependent cross-section are realized by $[\frac{\sigma}{m} = 18\frac{\text{cm}^2}{\text{g}}, w = 187.5684\frac{\text{km}}{\text{s}}]$ and $[\frac{\sigma}{m} = 90\frac{\text{cm}^2}{\text{g}}, w = 187.5684\frac{\text{km}}{\text{s}}]$. In figure 26 the core evolution of those isolated halos is shown. It can be seen that the core size r_{core} of the corresponding cross-sections fluctuates around each other, indicating that the core evolution is the same within numerical inaccuracies. As the core evolution

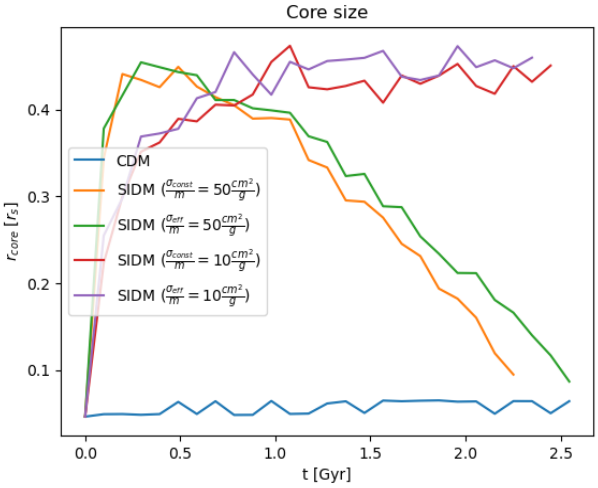

Figure 26: The core size r_{core} of isolated SIDM subhalos for two different constant cross sections and their corresponding velocity dependent cross section is shown.

advances in the core collapse phase the difference between the constant and the velocity dependent cross-section increases.

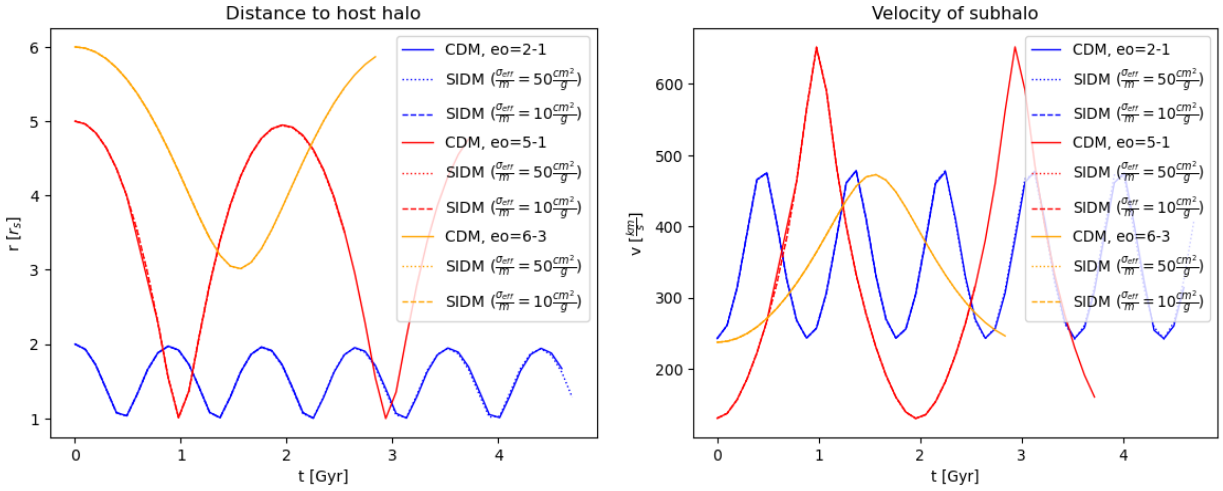

(a) (b)

Figure 27: (a) Radial distance of DM subhalos from the center of the DM host halo, shown for three distinct orbital configurations (orange, red, and blue).
(b) Velocities of the corresponding DM subhalos along the same orbital configurations.

4.3 Evolution of satellite galaxies

To qualitatively analyze the evolution of satellite galaxies, the focus is on satellite galaxies in Milky Way-mass systems. The following simulations model high-concentration DM subhalos with a virial mass of $M_{\text{vir}} = 10^{10} M_{\odot}$ within a DM host halo with a virial mass of $M_{\text{vir}} = 10^{13} M_{\odot}$.
The typical concentration for a halo of a given virial mass is determined using the concentration-mass relation, as described by the fit equation (3.12) in chapter 3.2.1. Concentration values for DM halos generally exhibit a variation of approximately 40% around the fit function. For the high-concentration DM subhalo, a concentration value 40% larger than the typical concentration is used. In contrast, the host halo is assigned the typical concentration, corresponding to the fit value for a halo with a virial mass of $M_{\text{vir}} = 10^{13} M_{\odot}$.
The chosen DM subhalo has a concentration of $c_{\text{vir}} = 30$, resulting in a scale density of $\rho_s = 0.0025 \frac{10^{10} M_{\odot}}{\text{kpc}^3}$ and a scale radius of $r_s = 1.52\,\text{kpc}$. These values characterize the DM subhalo's NFW density profile.
The host halo is assigned a typical concentration of $c_{\text{vir}} = 8.8$, yielding a scale density of $\rho_s = 0.00011 \frac{10^{10} M_{\odot}}{\text{kpc}^3}$ and a scale radius of $r_s = 51\,\text{kpc}$. These parameters define the NFW density profile of the DM host halo.

To qualitatively explore the evolution of DM subhalos, we focus on the critical influence of orbital parameters on their development. The distance of a DM subhalo's orbit from the host galaxy's center significantly affects the tidal forces it experiences. These tidal forces lead to notable variations in the evolution of DM subhalos, depending on their specific orbital characteristics.
To illustrate these effects, three distinct orbits, depicted in figure 27, are selected to highlight the

qualitative variations in possible subhalo evolutions. Those orbits are elliptical orbits (eo) and are label in figure 27 as "eo $= 2-1$", for example, which indicates an eo between $2r_s$ and r_s. The first orbit (blue), labeled as "eo $= 2-1$", remains consistently near to the host's center, with an apocenter of $r_{\text{apo}} = 2r_s$ and a pericenter of $r_{\text{peri}} = r_s$. The second orbit (red), labeled as "eo $= 5-1$", begins farther from the host's center, with an apocenter of $r_{\text{apo}} = 5r_s$, but still approaches as close as the first orbit at its pericenter of $r_{\text{peri}} = r_s$. The third orbit (orange), labeled as "eo $= 6-3$", starts even farther away and never approaches as closely as the other two orbits, with $r_{\text{apo}} = 6r_s$ and $r_{\text{peri}} = 3r_s$. Here the scale radius r_s correspond to the host halo.
These orbits provide a framework to analyze how varying orbital parameters affect the mass loss and structural evolution of DM subhalos.

Each orbit is simulated once for CDM (solid) and twice for SIDM (dotted, dashed), using two different velocity-dependent cross-sections. These cross-sections are characterized by the effective cross-sections for the subhalo, $\sigma_{\text{eff}} = [10\,\text{cm}^2/\text{g},\, 50\,\text{cm}^2/\text{g}]$. The lower effective cross-section $\sigma_{\text{eff}} = 10\,\text{cm}^2/\text{g}$ is represented by a dashed line and the higher effective cross-section $\sigma_{\text{eff}} = 50\,\text{cm}^2/\text{g}$ by a dotted line. The effective cross-section of the DM subhalo is realized by the two parameters for the velocity-dependent cross-sections $[\frac{\sigma}{m}, w]$. For the lower effective cross-section those parameters are $[\frac{\sigma}{m} = 18\frac{\text{cm}^2}{\text{g}},\ w = 187.5684\frac{\text{km}}{\text{s}}]$ and for the higher effective cross-section $[\frac{\sigma}{m} = 90\frac{\text{cm}^2}{\text{g}},\ w = 187.5684\frac{\text{km}}{\text{s}}]$. From figure 27 it can be seen that the corresponding CDM and SIDM subhalos have very similar orbits, eventho the SIDM subhalos experience evaporation.
First the evolution of CDM subhalos is analyzed. In the absence of external effects, CDM halos remain stable, as they are in gravitational equilibrium. For the CDM subhalos in this study, the only external influence considered is tidal forces, as dynamical friction has been neglected.
Then the evolution of SIDM subhalos is analyzed. Unlike CDM, SIDM halos evolve even in isolation due to self-interactions, which first lead to a core expansion phase followed by a core-collapse phase. When SIDM subhalos orbit a host halo, they are subjected to additional external effects, including tidal heating and evaporation. These external effects, combined with the internal processes of SIDM, result in complex evolution that differs significantly from their CDM counterparts.

4.3.1 CDM subhalo evolution

The gravitational potential of a CDM halo, presented in figure 4 of chapter 2.2.2, shows that gravitational forces decrease as the distance from the scale radius r_s increases. DM subhalo orbits are located at or beyond the scale radius r_s of the host halo. Consequently, DM subhalos closer to the scale radius r_s experience stronger tidal forces. These tidal forces are a key driver of mass loss in DM subhalos. The bound mass M_{bound} of CDM subhalos is depicted in the left panel of figure 28, where the curves correspond to different orbital configurations: the solid orange line represents the outermost orbit, the solid red line corresponds to the intermediate orbit, and the solid blue line shows the innermost orbit. As expected, the mass loss is greater for CDM subhalos with orbits closer to the center of the host halo.

For the CDM subhalo represented by the solid orange line, which initially orbits at $6r_s$, almost no mass is lost at this large radius. However, as the CDM subhalo moves closer to the host's center, significant mass loss occurs, peaking at the pericenter. Once the CDM subhalo moves back

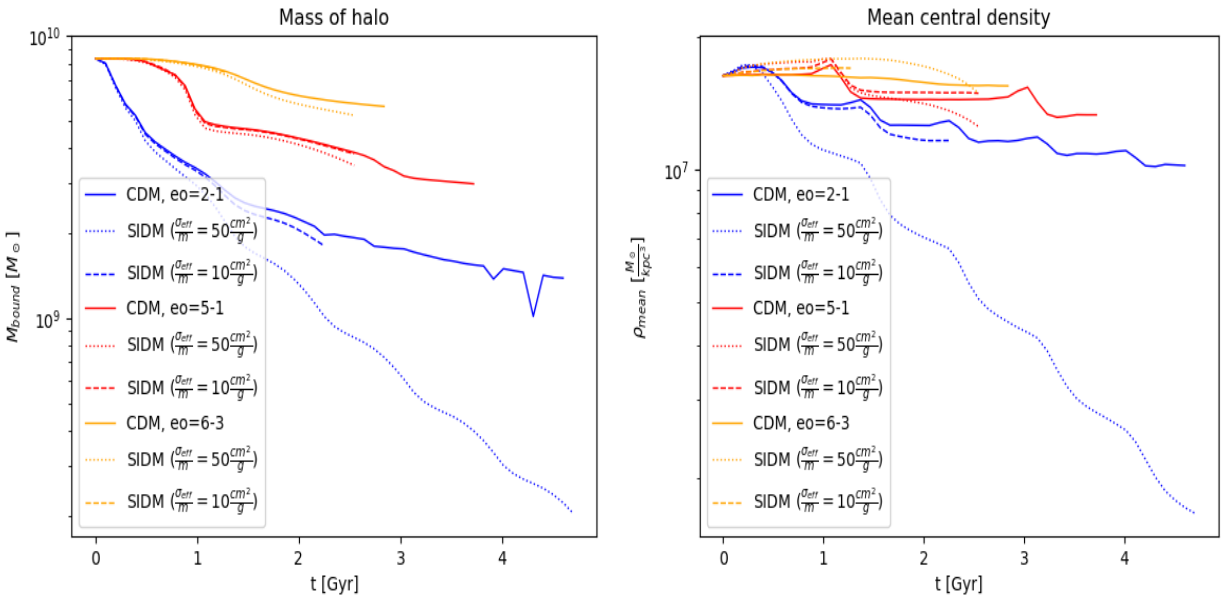

(a) (b)

Figure 28: (a) Evolution of the bound mass M_{bound} of DM subhalos for three distinct orbital configurations (orange, red and blue). Each orbital configuration is simulated once with CDM (solid) and twice with SIDM for two different velocity-dependent cross-sections (dashed, dotted). (b) Evolution of the mean central density ρ_{mean} of those DM subhalos, calculated within $2r_s$.

to the outer regions of its orbit, the mass loss decreases and eventually halts.
The red curve represents a CDM subhalo initially at $5r_s$. Similar to the orange curve, this CDM subhalo exhibits negligible mass loss at the apocenter of its orbit. However, as it approaches the pericenter, the mass loss begins earlier due to its closer orbit to the host's center. The total mass loss is larger compared to the orange curve because its orbit is overall closer to the host's center. After moving back to the apocenter, the mass loss almost vanishes, but it resumes with each return to the pericenter. Each subsequent pass results in less mass loss, indicating that the CDM subhalo approaches a stable bound mass M_{bound} over time.
For the CDM subhalo represented by the blue curve, which initially orbits at $2r_s$, significant mass loss occurs immediately due to the strong tidal forces at this radius. The difference in mass loss between the apocenter and pericenter is minimal, reflected only by small fluctuations in the bound mass M_{bound} curve. Over time, the CDM subhalo loses less mass with each orbit, eventually stabilizing at a constant bound mass M_{bound}. This trend is also observed for the other two orbits: with each pass near the pericenter, the CDM subhalo loses less mass until reaching a constant bound mass M_{bound}.

The right panel of figure 28 shows the mean central density ρ_{mean} of each DM subhalo within twice its scale radius r_s. For the CDM subhalo with the orange solid line, the mean central density ρ_{mean} remains constant during the early phases of its orbit, particularly at its apocenter ($r_{\text{apo}} = 6r_s$). This behavior mirrors that of isolated CDM halos.

For the red solid line, the mean central density ρ_{mean} is constant at first too. However, as the CDM subhalo approaches the pericenter, the subhalo experiences significant mass loss. The mean central density initially rises slightly, followed by a sharp drop. This response reflects how the inner structure reacts to tidal stripping. When the CDM subhalo moves back to the outer regions, the mean central density ρ_{mean} stabilizes.
The solid blue line follows a similar pattern. For CDM subhalos that lose more mass, the mean central density ρ_{mean} exhibits larger drops. However, as the CDM subhalo loses less mass over time, the subsequent decreases in the mean central density ρ_{mean} become smaller, ultimately stabilizing alongside the CDM subhalo's bound mass M_{bound}.

This analysis demonstrates the interplay between tidal forces, mass loss, and the internal density structure of CDM subhalos, highlighting the significant impact of orbital parameters on their evolution.

4.3.2 SIDM subhalo evolution

As previously discussed, SIDM subhalos with a core experience greater mass loss compared to those with a cuspy NFW profile. This increased mass loss occurs because core expansion reduces the central density ρ_{central} of the SIDM subhalo. A lower central density corresponds to a shallower gravitational potential, making it easier for particles to escape the SIDM subhalo. The evidence of this relationship that a core induces greater mass loss can be seen in figure 28, where SIDM subhalos consistently have a lower bound mass M_{bound} than their CDM counterparts.
The extent of mass loss in SIDM subhalos is strongly influenced by their orbital proximity to the host center. DM subhalos on closer orbits experience stronger tidal forces, which amplify the effects of core-induced mass loss. Therefore, the difference in mass loss between SIDM and CDM subhalos becomes more pronounced as the orbit brings the DM subhalo closer to the host center.
Core evolution plays a central role in this process. As the core expands, the gravitational potential becomes progressively shallower, enabling tidal forces to strip away more mass. SIDM subhalos with larger cores are particularly susceptible to mass loss since their reduced binding energy allows particles to escape more easily under the influence of tidal forces. Moreover, a prolonged core evolution phase exacerbates the mass loss, as the gravitational potential remains shallow for an extended period.
This dynamic relationship between core evolution, tidal forces, and mass loss underscores a key difference in the behavior of SIDM and CDM subhalos. While both are subject to tidal forces, the internal structure of SIDM subhalos renders them more vulnerable to these external effects, particularly on close orbits to the DM host halos center.
From figure 28, it can also be seen that the SIDM subhalos with the higher effective cross-section $\sigma_{\text{eff}} = 50\,\text{cm}^2/\text{g}$ consistently have a lower bound mass M_{bound} than their SIDM counterparts with the lower effective cross-section $\sigma_{\text{eff}} = 10\,\text{cm}^2/\text{g}$. This is most pronounced in the inner most orbit (blue lines), where the SIDM subhalo with the higher effective cross-section consistently loses a significant amount of mass.

Figure 29 illustrates the evolution of the core size r_{core} and the strongly correlated central density ρ_{central} for DM subhalos. CDM subhalos exhibit minimal core sizes r_{core}, which are primarily a

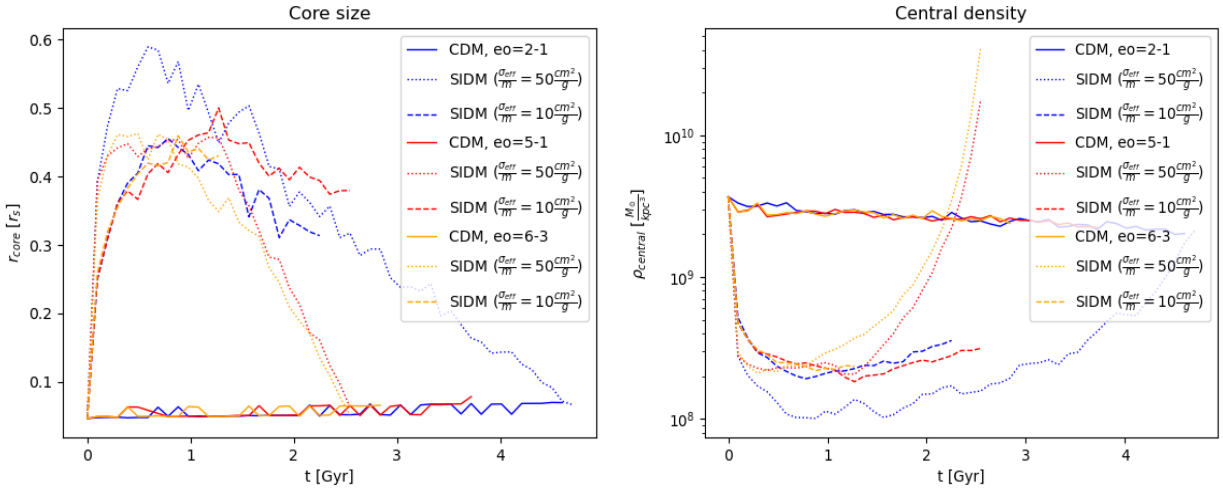

(a) (b)

Figure 29: (a) The evolution of the core size r_{core} of those DM subhalos for three distinct orbital configurations (orange, red and blue), each configuration once with CDM (solid) and for two different SIDM velocity dependent cross sections (dashed, dotted).
(b) The evolution of the central density ρ_{central} of those DM subhalos, calculated for the 1000 innermost particles.

result of numerical inaccuracies. Those numerical inaccuracies can lead to gravitational scatter events, which induce a small core. In contrast, SIDM subhalos exhibit a dynamic evolution, beginning with core expansion and transitioning to core collapse. The nature of this core evolution differs significantly depending on the SIDM subhalo's orbit within the DM host halo and the velocity-dependent cross-section.
The SIDM subhalos with the higher effective cross-section $\sigma_{\text{eff}} = 50\,\text{cm}^2/\text{g}$ evolve faster to their maximum core size and have an overall faster evolution of the core size r_s compared to the SIDM subhalos with the lower effective cross-section $\sigma_{\text{eff}} = 10\,\text{cm}^2/\text{g}$. This is shown for isolated SIDM subhalos in figure 26.
The SIDM subhalos with the higher effective cross-section also experience more evaporation scattering and can more efficiently inject energy into the SIDM subhalo from tidal heating.

The dotted and dashed orange line represents a SIDM subhalo on an orbit far from the host's center. The core size r_{core} and central density ρ_{central} of this SIDM subhalo evolve similarly to the corresponding isolated SIDM halo. This indicates that at this distance tidal effects do not significantly alter the internal structure or the core evolution of the SIDM subhalo. The core expands and eventually collapses in a manner consistent with an isolated system, largely unaffected by external forces. As the SIDM subhalo loses a small amount of mass, the core evolution is slightly accelerated compared to an isolated SIDM halo.
The dotted and dashed red line represents a SIDM subhalo on an intermediate orbit. Their core evolution diverges significantly from the corresponding orange curve between approximately 1.0 Gyr and 1.5 Gyr. At 1.0 Gyr, those SIDM subhalo reach their pericenter, where they experience strong

tidal forces. During this time, the SIDM subhalos also undergo substantial mass loss, primarily in their outer regions, as a result of these tidal forces.
Tidal forces can inject energy into a SIDM subhalo through tidal heating as a DM subhalo approaches close to the host's center. This injected energy delays the onset of the core collapse phase, as evidenced by the deviation of the dashed and dotted red curve from the dashed and dotted orange curve during this period. This can also be seen by comparing to the corresponding core evolution of the isolated SIDM halos in figure 26. Also evaporation contributes to the extended core size. Due to the increasing host density as the SIDM subhalo approaches its pericenter, the effect of evaporation is most significant at the pericenter. However, as those SIDM subhalos moves away from the host's center, the tidal heating and evaporation reduces, allowing the core collapse phase to commence around 1.5 Gyr. After this point, the core evolution of the dotted red curve almost converges with that of the corresponding dotted orange curve. This arises from the accelerated core evolution due to the mass loss. The dashed red curve goes faster into the core collapse phase as the corresponding isolated SIDM halo in figure 26.

The dotted and dashed blue line represents a SIDM subhalo on a close orbit, remaining near the host's center throughout its evolution. Unlike the other SIDM subhalos, this SIDM subhalo's core expansion is more immediate and significant, driven by continuous energy injection from tidal heating and by evaporation. This begins early in the evolution and persists, significantly altering the core's evolution.
Initially, the core size r_{core} expands further after the first pericenter passage. As the SIDM subhalo moves toward its apocenter, the core collapse phase begins. However, as the SIDM subhalo returns toward the pericenter, renewed energy injection from tidal heating and evaporation interrupts the core collapse phase, initiating a new core expansion phase. This cycle of core expansion at the pericenter and core collapse at the apocenter is constantly repeated.
Over time, this repeated pattern results in an extended core evolution for the dotted SIDM subhalo

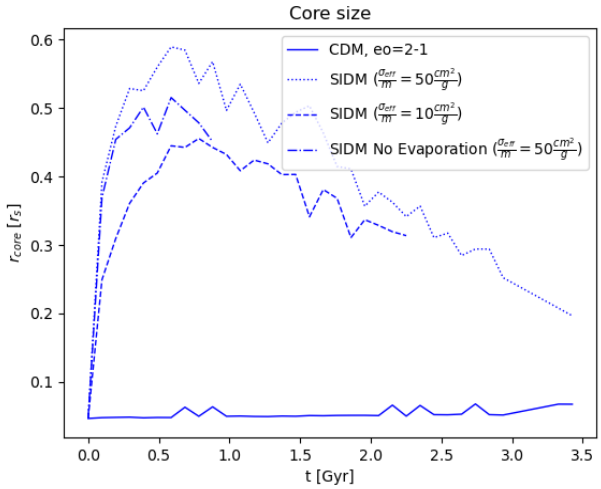

Figure 30: The core size r_{core} of DM subhalos for one orbital configuration. One CDM subhalo and three SIDM subhalos are shown. The SIDM subhalo with the larger effective cross-section is shown once with and without evaporation.

on the inner orbit. The injected energy from tidal heating and evaporation prolong the process, delaying the complete core collapse. However, the SIDM subhalo eventually appears to reach a point where the core fully collapses. The dashed SIDM subhalo goes faster into the core collapse phase as the corresponding isolated SIDM halo in figure 26.
To highlight the effects of tidal heating and evaporation, the SIDM subhalo on the innermost orbit with the high effective cross-section (dotted blue line) was also simulated without evaporation. This is shown in figure 30. It can be seen that without evaporation (dotted-dashed blue line) the tidal heating injects a large core size, but with evaporation this is even more significant.

As discussed in chapter 2.2.2, the temperature gradient is a key indicator of heat flow within a SIDM halo. It determines whether heat flows inward toward the core or outward from it. Figure 31 shows the evolution of the temperature gradient in the central region of the SIDM subhalos, specifically within $r \leq r_s$. On the left it is shown for the lower effective cross-section and on the right for the large effective cross-section. A positive temperature gradient signifies inward heat flow, which drives a core expansion phase. Conversely, a negative gradient indicates outward heat flow, leading to a core-collapse phase. By analyzing the temperature gradients of SIDM subhalos, we can understand how internal and external effects influence their core evolution.

The orange curve represents a SIDM subhalo with a core evolution similar to that of an isolated SIDM halo. Initially, the temperature gradient is strongly positive, indicating significant inward heat flow and driving a core expansion phase. Over time, the gradient approaches zero, signifying a thermalized state in the central region. Once thermal equilibrium is achieved, the gradient slowly becomes negative, marking the onset of the core collapse phase. This gradual transition highlights

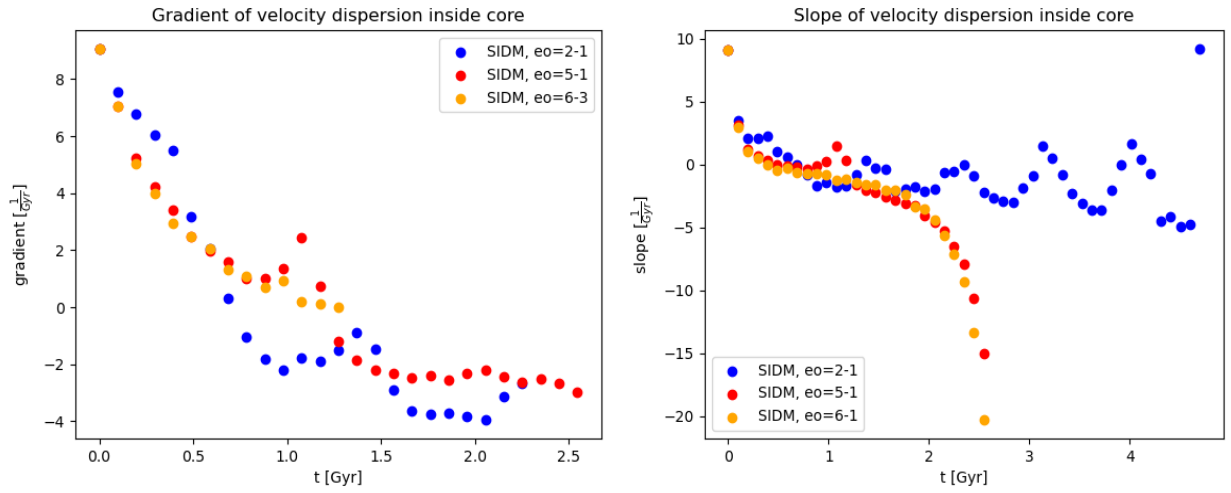

(a) (b)

Figure 31: The evolution of the gradient of the velocity dispersion inside the core of the SIDM subhalos, which indicate if the SIDM subhalo is in core expansion > 0 or core collapse phase < 0. The evolution of the gradient is shown for the SIDM subhalos with the lower effective cross section $\frac{\sigma_{\text{eff}}}{m} = 10\frac{\text{cm}^2}{\text{g}}$ (a) and the higher effective cross section $\frac{\sigma_{\text{eff}}}{m} = 50\frac{\text{cm}^2}{\text{g}}$ (b).

the expected evolution similar to an isolated SIDM halo. Therefore, the internal self-interactions dominate the internal dynamics. This is seen for both effective cross-sections.
The red curve shows the evolution of a SIDM subhalo on an intermediate orbit, where tidal forces play a significant role. During the core expansion phase, the temperature gradient evolves similarly to the orange curve, starting positive and gradually approaching zero. However, around 1.0 Gyr, the red curve shows a sudden increase in the temperature gradient, becoming positive again. This temporary rise indicates a short core expansion phase induced by tidal heating and evaporation. After this event, the temperature gradient turns negative, initiating the core collapse phase. This behavior demonstrates how tidal effects and evaporation can momentarily alter the heat flow within the SIDM subhalo, by inducing a core expansion phase. This is seen for both effective cross-sections.
The blue curve represents a SIDM subhalo on a close orbit, where tidal heating and evaporation are most pronounced. Initially, the central temperature gradient decreases, consistent with a core expansion phase. Around the SIDM subhalo's first pericenter, the temperature gradient deviates from the other SIDM subhalos, indicating an extended core expansion phase compared to the other two corresponding SIDM subhalos. This prolonged expansion results in a larger core size than that observed in an isolated SIDM halo (figure 26) or the other corresponding SIDM subhalos. By comparing the blue curves for the higher and the lower effective cross-section, it can be seen that the higher effective cross-section leads to stronger change in the temperature gradient. This is because the higher effective cross-section leads to a more efficient energy injection from tidal heating and more evaporation.
As the SIDM subhalo moves away from its pericenter, the temperature gradient decreases and becomes negative, signaling the beginning of a core-collapse phase. However, as the SIDM subhalo approaches its pericenter again, the temperature gradient turns positive for the higher effective cross-section, initiating another core expansion phase. The SIDM subhalo with the lower effective cross-section turns only almost positive, slowing down the core-collapse phase. This repeated alternation between expansion and collapse phases is driven by periodic tidal heating and evaporation. Over time, these cycles delay the core collapse, resulting in a more complex and extended evolution compared to SIDM subhalos on more distant orbits. Those cyclic increase of the temperature gradient becomes more significant with each cycle due to the progressing reduced bound mass M_{bound} of the SIDM subhalo.

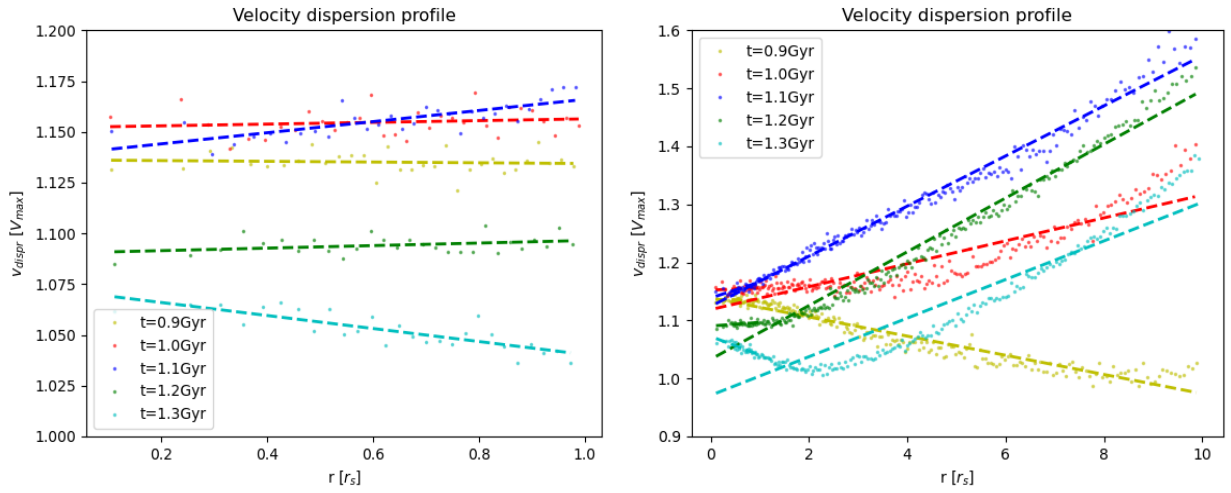

(a) (b)

Figure 32: The velocity dispersion profile v_{dispr} of the SIDM subhalo with an effective cross section of $\frac{\sigma_{\text{eff}}}{m} = 50\frac{\text{cm}^2}{\text{g}}$ on an elliptical orbit between $5r_s$ and $1r_s$. The profile is shown for 5 consecutive time steps (light green, red, blue, dark green and cyan).
(a) The velocity dispersion profile inside $1r_s$ with the simulated data (dots) and a linear fit function (dashed) to highlight the slope inside the core.
(b) The velocity dispersion profile inside $10r_s$ with the simulated data (dots) and a linear fit function (dashed) to highlight the slope at the outer regions.

4.3.3 Tidal heating

To gain a more detailed understanding of tidal heating, we focus on the SIDM subhalo corresponding to the red curve with the higher effective cross-section. This SIDM subhalo has reached it's maximum core size close before its first pericenter approach $t = 0.9$Gyr. This can be observed in figure 32, where the light green curve represents the temperature gradient at this time step. The left panel shows the central temperature gradients, while the right panel displays the overall gradients until $10r_s$. At this stage, the constant central gradient indicates that the SIDM subhalo has reached its maximum core size. The negative overall temperature gradient indicates that the SIDM subhalo has an heat flow outward and would go now over into the core collapse phase.
For the next time step $t = 1.0$Gyr (red curve), the central temperature gradient has increased from the light green to the red curve due to the heat flow outward (core collapse phase). For the red curve tidal forces strongly accelerate particles in the outer regions. This acceleration significantly increases the velocities in the outer regions compared to the rest of the halo. If the tidal forces are sufficiently strong, the temperature in the outer regions can surpass the temperature of the inner region. This is illustrated by the red curve in figure 32, which shows a large positive temperature gradient in the outer regions. Such a gradient indicates a heat flow from the outer regions into the inner regions. This is a characteristic signature of tidal heating.
The overall temperature gradient rises even more for the next time step $t = 1.1$Gyr (blue curve).

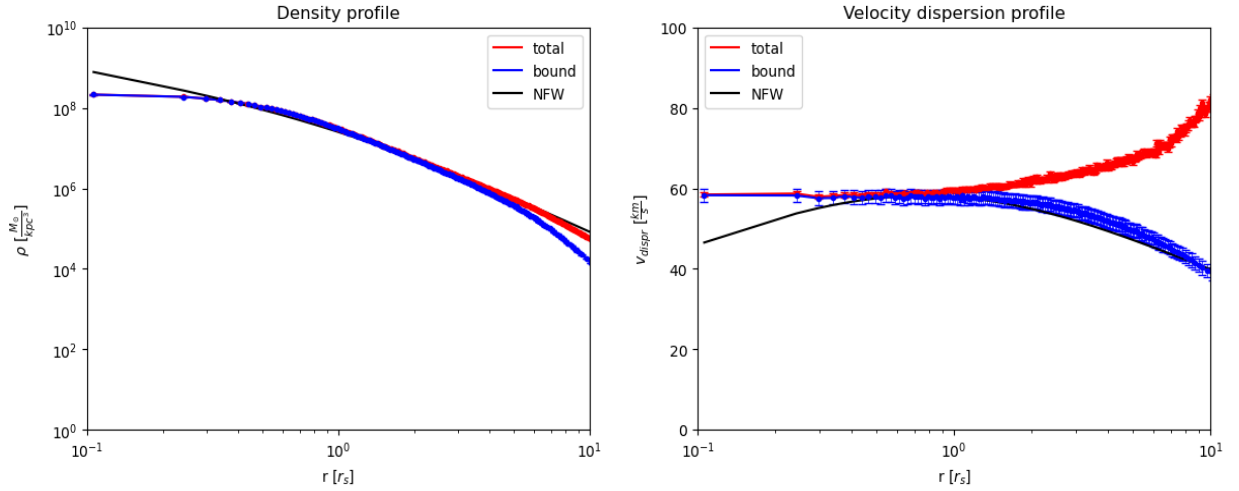

(a) $t = 1.1$Gyr (b) $t = 1.1$Gyr

Figure 33: (a) The density profile of the SIDM subhalo with an effective cross section of $\frac{\sigma_{\text{eff}}}{m} = 50\frac{\text{cm}^2}{\text{g}}$ on an elliptical orbit between $5r_s$ and $1r_s$. The profile is shown for all particles (red), for bound particles (blue), and is compared to the initial NFW profile (black).
(b) The corresponding velocity dispersion profile for all particles (red), for bound particles (blue), and compared to the initial NFW profile (black).

The central temperature gradient has developed a positive temperature gradient (core expansion phase).
For the next time step $t = 1.2$Gyr (green curve), the central temperature has decreased significant due to tidal heating and is almost constant. The overall temperature gradient is still positive.
For the last time step 1.3Gyr (cyan curve), the central temperature has further decreased due to tidal heating, but has now a negative temperature gradient. This indicates a heat flow outward from the center initiating a core collapse phase. The overall temperature gradient is still positive, but doesn't reach into the central region.

Figure 33 shows the density and velocity dispersion profiles during the moment when tidal heating occurs. These profiles distinguish between the total density/velocity dispersion and the bound density/velocity dispersion. The difference between the total and bound densities is most pronounced in the outer regions, highlighting the mass loss caused by tidal forces. As expected, this mass loss predominantly affects the DM subhalo's outer regions.
The difference between the total and bound velocity dispersions further illustrates the impact of tidal heating. The stripped particles, with their high velocities, contribute to tidal heating by inducing a positive temperature gradient. However, the bound particles in these regions do not contribute to the positive gradient. This difference between the total and bound particles in the velocity dispersion underscores the key role of stripped particles in driving tidal heating and shaping the SIDM subhalo's evolution.

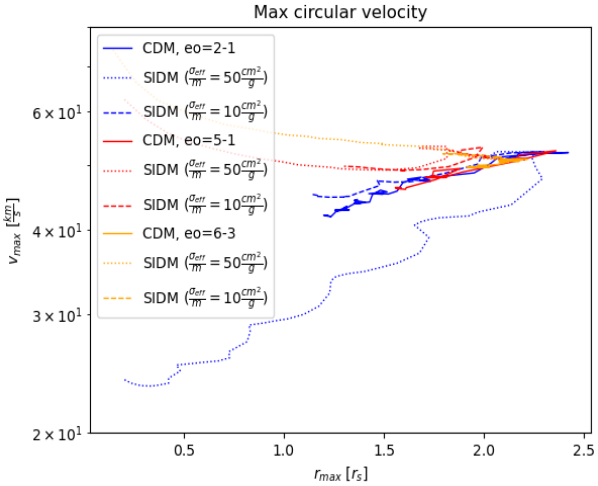

Figure 34: The maximum circular velocity $v_{\max}$ and the corresponding radius $r_{\max}$ of the DM subhalos.

4.3.4 Maximum circular velocity

A particularly insightful observable for characterizing DM subhalos is the maximum circular velocity $v_{\max}$ and the radius $r_{\max}$ where it occurs. The evolution of this observable is depicted in figure 31.
By comparing the CDM subhalos (solid line) with the SIDM subhalos (dotted and dashed lines), it can be seen that the SIDM subhalos can exhibit a much larger variation of the maximum circular velocity $v_{\max}$ and its corresponding radius $r_{\max}$.

The dotted and dashed orange curves represent a SIDM subhalo on a relatively distant orbit. Initially, the SIDM subhalos maximum circular velocity evolves by gradually moving inward, causing a decrease in $r_{\max}$. During this phase, $v_{\max}$ increases slowly at first but grows more rapidly as $r_{\max}$ continues to shrink.
The dotted and dashed red curve begin with a similar evolution to the orange curves, as $r_{\max}$ decreases and $v_{\max}$ increases slowly. However, when $r_{\max}$ reaches approximately $1.5r_s$, the trend reverses: $r_{\max}$ begins to increase, followed by a noticeable decrease in $v_{\max}$. This turning point coincides with a significant mass loss of the SIDM subhalo. The loss of mass causes a substantial drop in $v_{\max}$. Beyond this point, the red curves evolves almost parallel to the orange curves but with a consistently lower $v_{\max}$, reflecting the diminished mass of the SIDM subhalo.
The dotted and dashed blue curve exhibits a markedly different evolution due to the SIDM subhalo's immediate significant mass loss. This behavior results from the close proximity of the SIDM subhalo's orbit to the host's center. Around each pericenter passage, the SIDM subhalo experiences a sharp drop in $v_{\max}$, reflecting the intense tidal stripping at these points. Conversely, around each apocenter, the mass loss and corresponding change in $v_{\max}$ and $r_{\max}$ are less pronounced. As the dashed blue line looses less mass over time, the dotted blue line deviates stronger from the other lines. Over time, $r_{\max}$ gradually decreases, a trend observed in all DM subhalos.

These curves collectively illustrate how the DM subhalo's orbit shapes the evolution of key dynamical properties. $v_{\max}$ and $r_{\max}$ provide critical insights into the structural changes driven by all the effects that influence the DM subhalo.

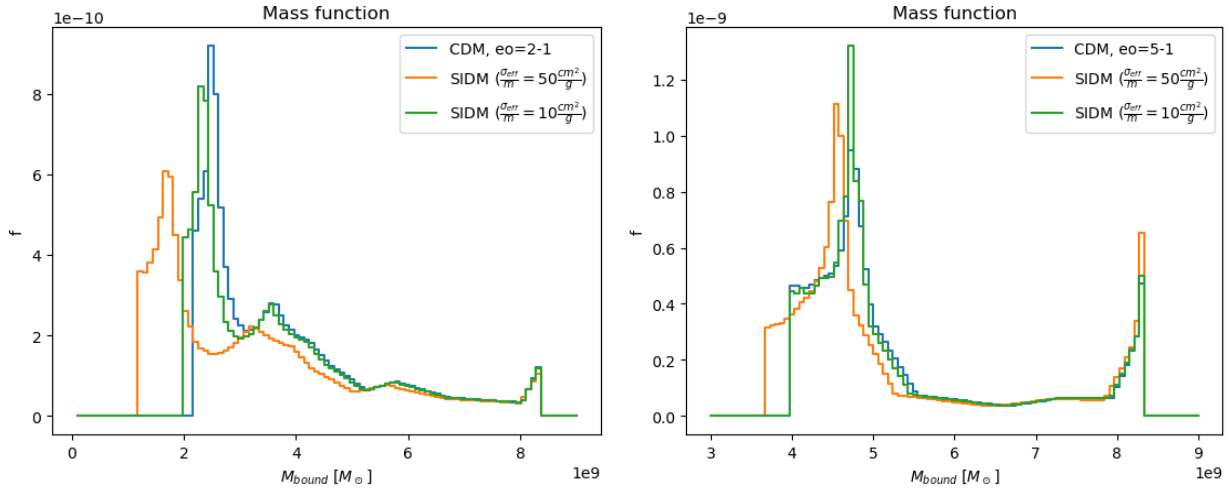

(a) (b)

Figure 35: The DM subhalo mass functions are shown for two distinct orbital configuration and compares the CDM (blue) and the two SIDM cross sections (green and orange).
(a) The subhalo mass function for the elliptical orbit between $2r_s$ and r_s.
(b) The subhalo mass function for the elliptical orbit between $5r_s$ and r_s.

4.3.5 DM subhalo mass function

The DM subhalo mass function describes the mass distribution of DM subhalos within a host system. This metric is of particular interest because it provides a straightforward way to compare simulations with observations. By analyzing the observed mass distribution of DM subhalos and comparing it to simulation results, the validity of different DM models can be assessed statistically. However, this thesis focus is exclusively on satellite galaxies, all simulated with identical concentrations and virial masses. Additionally, the orbital selection used in the simulations introduces a bias that does not reflect the expected natural distribution of DM subhalo orbits. Since orbital parameters strongly influence the extent of mass loss in DM subhalos, the subhalo mass function derived here cannot be directly compared with observed DM subhalo mass functions. Instead, this thesis uses the subhalo mass function as a tool to qualitatively examine how SIDM alters the mass distribution of DM subhalos compared to CDM. Additionally, the impact of varying self-interaction cross-sections on the mass function is investigated.
To facilitate comparisons between CDM and the two SIDM models, the subhalo mass function is plotted for two orbital scenarios. Those are shown in figure 35. The left panel of the figure shows the mass function for the innermost orbit. For this orbit, DM subhalos experience an immediate and substantial mass loss, which gradually slows down over time. This leads to a mass function that favors DM subhalos with significantly lower masses than their initial values. For CDM subhalos, the mass function shows a sharp peak. SIDM subhalos initially follow a similar trend, but their mass functions rise more slowly and reach later their peaks. The SIDM subhalo with the larger effective cross-section (orange) deviates stronger from the CDM subhalo.
A similar trend is observed for the next orbit (right panel), which is farther from the center of the

host. Both CDM and SIDM subhalos evolve similarly at first, but the CDM subhalo mass function starts increasing earlier and reaches a peak earlier. In contrast, the SIDM subhalos mass functions increase a bit slower and reach their peak slightly later. Again the SIDM subhalo with the larger effective cross-section (orange) deviates more from the CDM subhalo.
From these results, evidence that SIDM models predict a higher prevalence of DM subhalos with lower masses compared to CDM is shown. Furthermore, the closer a subhalo's orbit is to the center of the host galaxy, the greater the expected difference between the predictions of CDM and SIDM. This makes observations of satellite galaxies near the scale radius of the host system particularly valuable for testing DM models. These satellites are key systems for examining the mass loss behavior that distinguishes SIDM from CDM.

5 Discussion and limitations

This thesis primarily focuses on the qualitative investigation of DM subhalo evolution with the N-body code OpenGadget3. The host system is represented using an analytic potential of a DM halo. The stellar components were not included for the host and satellite system. This allows for a focused study on the interaction between DM subhalos and their DM host halos. The stellar components of the host can play a significant role in the overall evolution of a DM subhalo and should not be ignored in a more realistic model.
For SIDM, the host halo would also evolve from its initial NFW profile due to self-interactions among DM particles. However, the significantly higher relative velocities in the host halo compared to the subhalo result in a much lower probability of scattering events for a velocity-dependent cross-section. Consequently, the host halo evolves more slowly, and the formation of a core in its central region ($r \ll r_s$) is minimal over the timescales considered in this study. While this slower evolution implies that the analytic NFW potential used in this thesis does not precisely capture the host halo's inner regions for SIDM, it accurately represents the outer regions where satellite galaxies typically orbit. Therefore, using an analytic NFW profile for the host DM halo is a reasonable approximation for our purposes.

The evaporation scattering routine implemented in this thesis accounts for three of the four possible scattering scenarios. Two scenarios are naturally included: (1) both particles become unbound, and (2) the SIDM subhalo particle remains bound while the SIDM host halo particle remains unbound. A third scenario—where the SIDM subhalo particle becomes unbound, and the host halo particle becomes bound—has also been implemented and tested. It was found that neglecting this scenario introduces a relative error of only a few percent in the SIDM subhalo's mass loss for the given simulation (shown in chaper 4.1.2). However, the fourth scenario, where both particles remain bound after scattering, has not yet been implemented. This scenario is expected to have a similar impact on the mass loss as the third scenario and should be explored to determine whether its inclusion significantly improves accuracy.
The virtual host particles used in the evaporation routine were sampled using the Eddington inversion method, ensuring a realistic representation of the local environment. Currently, this method is applied under the assumption of a spherically symmetric host's density profile. However, if the host system includes a stellar disc, this would break the assumption of spherical symmetry and alter the local velocity distribution of DM particles. Extending the Eddington inversion method to accommodate non-spherical symmetry would allow for a more comprehensive analysis. Investigating the effects of such refinements could be a focus for future work.

Another discussion involves the velocity-dependent cross-section used in the SIDM models. In this thesis, the effective cross-section for the halo is set to match the constant cross-section at the initial characteristic velocity dispersion $\sigma_{\text{eff}}^{\text{1D}}$. This ensures that the initial evolution of the halo closely resembles that of a constant cross-section model. However, as the halo evolves and its characteristic velocity dispersion changes, the effective cross-section diverges from the constant value. Calculating the effective cross-section based on the velocity dispersion at the halo's maximum core size could potentially improve the accuracy of the model. This approach could be explored further to assess its impact.

Dynamical friction, which slows down the motion of DM subhalos was neglected in this study. For the subhalo masses considered ($m_{\text{sub}} \leq \frac{1}{1000} m_{\text{host}}$), this omission is justifiable, as the impact of dynamical friction is minimal. However, accurately simulating more relatively massive DM subhalos would require the inclusion of dynamical friction.

The framework developed in this thesis has been used to qualitatively study DM subhalo evolution, but it could also be applied to compare simulation results with observational data. For example, the DM subhalo mass function could be used as a statistical observable for validating DM models. To achieve this, it would be necessary to sample DM subhalo orbits from a realistic distribution [84], accounting for variations in DM subhalo mass, concentration, and infall time. Also the SIDM subhalo could have already a core, when it becomes bound to the host system. In this thesis the SIDM subhalos are initially without a core. Producing a robust DM subhalo mass function would require running a large number of simulations. Developing a semi-analytic model for DM subhalo evolution, validated against this framework, could make such studies even more computationally efficient.
Another useful observable is the spatial distribution of DM subhalos within the host. This distribution is strongly influenced by the biased orbits in this thesis and would require the inclusion of a realistic orbital distribution for meaningful comparisons with observations. Similar to the DM subhalo mass function, this observable could be studied using a combination of simulations and semi-analytic models.

For individual satellite galaxies, properties such as the maximum circular velocity and the radius at which it occurs are critical for comparisons between simulations and observations. Satellite galaxies are only observed in their current state, making it challenging to reconstruct their evolution. Simulations must test a range of initial configurations and orbital parameters to identify ICs that evolve to match the observed properties [85]. A semi-analytic model could streamline this process by providing a more efficient way to explore the parameter space.
Finally, the projected mass and density slope of DM subhalos along the line of sight could be compared with observations derived from perturbed gravitational lensing. This approach, however, faces the same challenge of requiring many simulations to match individual satellite galaxies. Semi-analytic models could improve the efficiency of such comparisons.

6 Conclusion

This thesis qualitatively investigated the evolution of satellite galaxies, focusing on the DM halos of both satellites and their host galaxies. The study compared the predictions of CDM and SIDM models, particularly examining how the cross-section for SIDM influences DM subhalo evolution.
The velocity-dependent cross-section for SIDM, already motivated by constraints on effective cross-sections, was shown to play a critical role in enabling a core-collapse phase. This feature is not achievable with a constant cross-section, making the velocity-dependent cross-section essential for addressing the diversity problem observed in CDM subhalos. The interplay between core expansion and collapse phases is vital for explaining the varied inner density profiles of satellite galaxies.
CDM subhalos primarily lose mass through tidal forces, which strip particles from their outer regions while leaving the inner structure largely intact. In contrast, SIDM subhalos experience additional mass loss due to their core structure, as well as evaporation effects absent in CDM subhalos. The inner structure of SIDM subhalos evolves under the influence of multiple factors, including tidal forces, tidal heating, evaporation, and core dynamics, with their evolution varying significantly based on orbital parameters.
Mass loss from tidal forces accelerates the core evolution of a SIDM subhalo compared to an isolated SIDM halo. However, tidal heating, which injects energy into the SIDM subhalo, can induce a core expansion phase or halt a core-collapse phase, effectively slowing the overall evolution of the core. Additionally evaporation can induce a core expansion phase or halt a core-collapse phase. The combined effects of tidal heating, evaporation and mass loss are strongly influenced by the DM subhalo's orbital proximity to the DM host center, resulting in a dependence of the core expansion and collapse durations on the DM subhalo's orbit.
A higher effective cross-section for SIDM subhalos accelerates core evolution by enhancing self-interactions. However, it also amplifies the energy injected through tidal heating (discussed in chapter 4.3.2) and the evaporation effect, which counteracts this acceleration by slowing the progression of the overall core evolution. As a result, the interplay between these effects means that each SIDM subhalo must be considered individually to determine whether its core evolution is faster or slower than that of a corresponding isolated SIDM halo.
Fluid models, such as the Nishikawa Code [21], predict accelerated core evolution due to tidal mass loss but cannot capture all relevant effects. This highlights the necessity of using N-body simulations for studying DM subhalos, as they provide a more comprehensive framework for modeling the complex dynamics involved.

7 Outlook

This thesis established a framework for modeling the complex dynamics of DM subhalos. While its primary focus has been on the qualitative study of DM subhalo evolution, the framework holds significant potential for future applications.

As discussed in chapter 5, there are multiple possible improvements of the framework. Some of those are the implementation of the missing scenario for the evaporation routine, the implementation of dynamical friction and extending the Eddington Inversion to non-spherical symmetric systems.

So far, the SIDM subhalos were only simulated with an isotropic cross-section. As alternative angular dependent cross-sections can already be simulated within OpenGadget3, it would be exciting to investigate how the angular dependency of self-interactions can influence the evolution of SIDM subhalos.

An exciting next step would be to compare the simulated properties of satellite galaxies with their observed counterparts. As discussed in the chapter 1, a substantial number of satellite galaxies have already been observed, and upcoming surveys will provide even more data.

A variety of observables can be leveraged to study DM models, spanning both individual satellite properties and broader population distributions. For individual satellites, key observables include the maximum circular velocity and its corresponding radius. Additionally, projected mass and density slopes derived from perturbed gravitational lensing present intriguing opportunities for comparison. The satellite mass function and the spatial distribution of satellites within host systems serve as critical metrics for testing DM models.

To effectively utilize these observables, a significant number of simulations will be required. Developing a semi-analytic model could address this challenge by enabling a much larger volume of simulations at a reduced computational cost [27, 86]. Such a model could be constructed and validated using the N-body simulation framework developed in this thesis, ensuring its accuracy and reliability.

Once established, this semi-analytic model could be integrated with techniques such as Markov Chain Monte Carlo (MCMC) to perform joint fits across all relevant observables. This approach would provide robust constraints on the SIDM cross-section, advancing our understanding of DM models and their implications for the evolution of satellite galaxies.

Acknowledgments

I would like to express my sincere gratitude to Prof. Dr. Laura Sagunski and Dr. Moritz Fischer for their invaluable guidance, support, and collaboration over the past year, as well as for introducing me to this fascinating field of research.
I am also deeply thankful to Prof. Dr. Manoj Kaplinghat and Prof. Dr. Kimberly Boddy for their insightful input and discussions, which significantly contributed to the development of this work.

A special thank you goes to my wife, Coco, for her unwavering support and encouragement in every possible way. I also extend my heartfelt thanks to my friends and family for their constant help and encouragement.

Selbständigkeitserklärung

Hiermit erkläre ich, dass ich die Arbeit selbstständig und ohne Benutzung anderer als der angegebenen Quellen und Hilfsmittel verfasst habe. Alle Stellen der Arbeit, die wörtlich oder sinngemäß aus Veröffentlichungen oder aus anderen fremden Texten entnommen wurden, sind von mir als solche kenntlich gemacht worden. Ferner erkläre ich, dass die Arbeit nicht - auch nicht auszugsweise - für eine andere Prüfung verwendet wurde.

Ort, Datum: Unterschrift:

Bibliography

[1] S. Alam *et al.* (BOSS), Mon. Not. Roy. Astron. Soc. **470**, 2617 (2017), arXiv:1607.03155 [astro-ph.CO] .

[2] R. E. Angulo and O. Hahn, Living Reviews in Computational Astrophysics **8** (2022), 10.1007/s41115-021-00013-z.

[3] T. Ishiyama, The Astrophysical Journal **788**, 27 (2014).

[4] R. H. Wechsler and J. L. Tinker, ARA&A **56**, 435 (2018), arXiv:1804.03097 [astro-ph.GA] .

[5] S. Tulin and H.-B. Yu, Phys. Rept. **730**, 1 (2018), arXiv:1705.02358 [hep-ph] .

[6] S. Adhikari *et al.*, (2022), arXiv:2207.10638 [astro-ph.CO] .

[7] M. Kaplinghat, S. Tulin, and H.-B. Yu, Phys. Rev. Lett. **116**, 041302 (2016), arXiv:1508.03339 [astro-ph.CO] .

[8] O. D. Elbert, J. S. Bullock, M. Kaplinghat, S. Garrison-Kimmel, A. S. Graus, and M. Rocha, The Astrophysical Journal **853**, 109 (2018).

[9] L. Sagunski, S. Gad-Nasr, B. Colquhoun, A. Robertson, and S. Tulin, JCAP **01**, 024 (2021), arXiv:2006.12515 [astro-ph.CO] .

[10] K. E. Andrade, J. Fuson, S. Gad-Nasr, D. Kong, Q. Minor, M. G. Roberts, and M. Kaplinghat, Mon. Not. Roy. Astron. Soc. **510**, 54 (2021), arXiv:2012.06611 [astro-ph.CO] .

[11] L. Ackerman, M. R. Buckley, S. M. Carroll, and M. Kamionkowski, Phys.Rev. **D79**, 023519 (2009), arXiv:0810.5126 [hep-ph] .

[12] J. L. Feng, M. Kaplinghat, and H.-B. Yu, Phys. Rev. Lett. **104**, 151301 (2010), arXiv:0911.0422 [hep-ph] .

[13] A. Loeb and N. Weiner, Phys. Rev. Lett. **106**, 171302 (2011), arXiv:1011.6374 [astro-ph.CO] .

[14] M. R. Buckley and P. J. Fox, Phys. Rev. **D81**, 083522 (2010), arXiv:0911.3898 [hep-ph] .

[15] T. Lin, H.-B. Yu, and K. M. Zurek, Phys.Rev. **D85**, 063503 (2012), arXiv:1111.0293 [hep-ph] .

[16] J. M. Cline, Z. Liu, G. Moore, and W. Xue, Phys. Rev. D **89**, 043514 (2014), arXiv:1311.6468 [hep-ph] .

[17] J. M. Cline, Z. Liu, G. D. Moore, and W. Xue, Phys. Rev. D **90**, 015023 (2014), arXiv:1312.3325 [hep-ph] .

[18] K. K. Boddy, J. L. Feng, M. Kaplinghat, and T. M. P. Tait, Phys. Rev. D **89**, 115017 (2014), arXiv:1402.3629 [hep-ph] .

[19] B. Colquhoun, S. Heeba, F. Kahlhoefer, L. Sagunski, and S. Tulin, Phys. Rev. D **103**, 035006 (2021), arXiv:2011.04679 [hep-ph] .

[20] O. D. Elbert, J. S. Bullock, S. Garrison-Kimmel, M. Rocha, J. Oñorbe, and A. H. G. Peter, Mon. Not. Roy. Astron. Soc. **453**, 29 (2015), arXiv:1412.1477 [astro-ph.GA] .

[21] H. Nishikawa, K. K. Boddy, and M. Kaplinghat, Phys. Rev. D **101**, 063009 (2020), arXiv:1901.00499 [astro-ph.GA] .

[22] F. Kahlhoefer, M. Kaplinghat, T. R. Slatyer, and C.-L. Wu, JCAP **12**, 010 (2019), arXiv:1904.10539 [astro-ph.GA] .

[23] J. Zavala and C. S. Frenk, Galaxies **7**, 81 (2019), arXiv:1907.11775 [astro-ph.CO] .

[24] M. Kaplinghat, M. Valli, and H.-B. Yu, Mon. Not. Roy. Astron. Soc. **490**, 231 (2019), arXiv:1904.04939 [astro-ph.GA] .

[25] C. A. Correa, Mon. Not. Roy. Astron. Soc. **503**, 920 (2021), arXiv:2007.02958 [astro-ph.GA] .

[26] H. C. Turner, M. R. Lovell, J. Zavala, and M. Vogelsberger, Mon. Not. Roy. Astron. Soc. **505**, 5327 (2021), arXiv:2010.02924 [astro-ph.GA] .

[27] O. Slone, F. Jiang, M. Lisanti, and M. Kaplinghat, Phys. Rev. D **107**, 043014 (2023), arXiv:2108.03243 [astro-ph.CO] .

[28] Z. C. Zeng, A. H. G. Peter, X. Du, A. Benson, S. Kim, F. Jiang, F.-Y. Cyr-Racine, and M. Vogelsberger, Mon. Not. Roy. Astron. Soc. **513**, 4845 (2022), arXiv:2110.00259 [astro-ph.CO] .

[29] I. Dutra, P. Natarajan, and D. Gilman, (2024), arXiv:2406.17024 [astro-ph.CO] .

[30] M. S. Fischer, K. Dolag, and H.-B. Yu, Astron. Astrophys. **689**, A300 (2024), arXiv:2403.00739 [astro-ph.CO] .

[31] S. Gad-Nasr, K. K. Boddy, M. Kaplinghat, N. J. Outmezguine, and L. Sagunski, JCAP **05**, 131 (2024), arXiv:2312.09296 [astro-ph.GA] .

[32] C. Mace, Z. C. Zeng, A. H. G. Peter, X. Du, S. Yang, A. Benson, and M. Vogelsberger, (2024), arXiv:2402.01604 [astro-ph.GA] .

[33] I. Palubski, O. Slone, M. Kaplinghat, M. Lisanti, and F. Jiang, JCAP **09**, 074 (2024), arXiv:2402.12452 [astro-ph.CO] .

[34] N. Shah and S. Adhikari, Mon. Not. Roy. Astron. Soc. **529**, 4611 (2024), arXiv:2308.16342 [astro-ph.CO] .

[35] V. Tran, D. Gilman, M. Vogelsberger, X. Shen, S. O'Neil, and X. Zhang, Phys. Rev. D **110**, 043048 (2024), arXiv:2405.02388 [astro-ph.GA] .

[36] Z. C. Zeng, A. H. G. Peter, X. Du, S. Yang, A. Benson, F.-Y. Cyr-Racine, F. Jiang, C. Mace, and R. B. Metcalf, (2023), arXiv:2310.09910 [astro-ph.GA] .

[37] X. Zhang, H.-B. Yu, D. Yang, and E. O. Nadler, (2024), arXiv:2409.19493 [astro-ph.GA] .

[38] Y.-M. Zhong, D. Yang, and H.-B. Yu, Mon. Not. Roy. Astron. Soc. **526**, 758 (2023), arXiv:2306.08028 [astro-ph.CO] .

[39] O. Slone, F. Jiang, M. Lisanti, and M. Kaplinghat, "Orbital evolution of satellite galaxies in self-interacting dark matter models," (2023), arXiv:2108.03243 [astro-ph.CO] .

[40] Y.-Y. Mao *et al.*, (2024), arXiv:2404.14498 [astro-ph.GA] .

[41] T. Prusti *et al.* (Gaia), Astron. Astrophys. **595**, A1 (2016), arXiv:1609.04153 [astro-ph.IM] .

[42] v. Ivezić *et al.* (LSST), Astrophys. J. **873**, 111 (2019), arXiv:0805.2366 [astro-ph] .

[43] Q. E. Minor, S. Gad-Nasr, M. Kaplinghat, and S. Vegetti, Mon. Not. Roy. Astron. Soc. **507**, 1662 (2021), arXiv:2011.10627 [astro-ph.GA] .

[44] Q. E. Minor, "High detection significance of the dark substructure in gravitational lens sdssj0946+1006 is revealed by image pixel supersampling," (2024), arXiv:2408.11090 [astro-ph.GA] .

[45] M. Barry, A. Wetzel, S. Chapman, J. Samuel, R. Sanderson, and A. Arora, Mon. Not. Roy. Astron. Soc. **523**, 428 (2023), arXiv:2303.05527 [astro-ph.GA] .

[46] F. Groth, U. P. Steinwandel, M. Valentini, and K. Dolag, Mon. Not. Roy. Astron. Soc. **526**, 616 (2023), arXiv:2301.03612 [astro-ph.IM] .

[47] M. S. Fischer, M. Brüggen, K. Schmidt-Hoberg, K. Dolag, F. Kahlhoefer, A. Ragagnin, and A. Robertson, Monthly Notices of the Royal Astronomical Society **505**, 851 (2021), https://academic.oup.com/mnras/article-pdf/505/1/851/38378730/stab1198.pdf .

[48] M. S. Fischer, M. Brüggen, K. Schmidt-Hoberg, K. Dolag, A. Ragagnin, and A. Robertson, Monthly Notices of the Royal Astronomical Society **510**, 4080 (2021), https://academic.oup.com/mnras/article-pdf/510/3/4080/42194749/stab3544.pdf .

[49] Z. C. Zeng, A. H. G. Peter, X. Du, A. Benson, S. Kim, F. Jiang, F.-Y. Cyr-Racine, and M. Vogelsberger, "Core-collapse, evaporation and tidal effects: the life story of a self-interacting dark matter subhalo," (2021), arXiv:2110.00259 [astro-ph.CO] .

[50] J. H. Oort, ApJ **91**, 273 (1940).

[51] F. Zwicky, Helvetica Physica Acta **6**, 110 (1933).

[52] V. C. Rubin, J. Ford, W. K., and N. Thonnard, ApJ **238**, 471 (1980).

[53] M. D. Leo, "Rotation curve of spiral galaxy messier 33 (triangulum)," (2018), accessed: 2025-01-02.

[54] R. V. Wagoner, Astrophys. J. **179**, 343 (1973).

[55] C. X. ray Observatory, "1e 0657-56, "bullet cluster"," (2006), credit: X-ray: NASA/CXC/CfA/M.Markevitch et al.; Optical: NASA/STScI; Magellan/U.Arizona/D.Clowe et al.; Lensing Map: NASA/STScI; ESO WFI; Magellan/U.Arizona/D.Clowe et al., accessed: 2025-01-02.

[56] S. W. Randall, M. Markevitch, D. Clowe, A. H. Gonzalez, and M. Bradač, The Astrophysical Journal **679**, 1173–1180 (2008).

[57] M. C. 2dF Galaxy Redshift Survey, "2dfzcone," (2003), accessed: 2025-01-02.

[58] N. A. Bahcall, J. P. Ostriker, S. Perlmutter, and P. J. Steinhardt, Science **284**, 1481 (1999), arXiv:astro-ph/9906463 [astro-ph] .

[59] E. Rebhan, *Theoretische Physik: Relativitätstheorie und Kosmologie*, Theoretische Physik / Eckhard Rebhan (Spektrum Akademischer Verlag, 2011).

[60] W. J. G. de Blok, Adv. Astron. **2010**, 789293 (2010), arXiv:0910.3538 [astro-ph.CO] .

[61] A. Zentner, S. Dandavate, O. Slone, and M. Lisanti, Journal of Cosmology and Astroparticle Physics **2022**, 031 (2022).

[62] J. S. Bullock, "Notes on the missing satellites problem," (2010), arXiv:1009.4505 [astro-ph.CO] .

[63] F. Jiang and F. C. van den Bosch, Monthly Notices of the Royal Astronomical Society **453**, 3576–3593 (2015).

[64] G. Ogiya and M. Mori, The Astrophysical Journal **793**, 46 (2014).

[65] M. R. Lovell, V. Gonzalez-Perez, S. Bose, A. Boyarsky, S. Cole, C. S. Frenk, and O. Ruchayskiy, Monthly Notices of the Royal Astronomical Society **468**, 2836–2849 (2017).

[66] B. Colquhoun, S. Heeba, F. Kahlhoefer, L. Sagunski, and S. Tulin, Phys. Rev. D **103**, 035006 (2021).

[67] J. E. Taylor, Advances in Astronomy **2011**, 1–17 (2011).

[68] J. Binney and S. Tremaine, *Galactic Dynamics: Second Edition*, Princeton Series in Astrophysics (Princeton University Press, 2011).

[69] J. F. Navarro, C. S. Frenk, and S. D. M. White, Astrophys. J. **490**, 493 (1997), arXiv:astro-ph/9611107 [astro-ph] .

[70] D. Yang, E. O. Nadler, H.-B. Yu, and Y.-M. Zhong, Journal of Cosmology and Astroparticle Physics **2024**, 032 (2024).

[71] M. F. Darkium, "Compilation of sidm constraints," (2025), accessed: 2025-01-02.

[72] M. S. Fischer, L. Kasselmann, M. Brüggen, K. Dolag, F. Kahlhoefer, A. Ragagnin, A. Robertson, and K. Schmidt-Hoberg, Monthly Notices of the Royal Astronomical Society **529**, 2327–2348 (2024).

[73] N. C. Amorisco, "Cold dark matter subhaloes at arbitrarily low masses," (2021), arXiv:2111.01148 [astro-ph.CO] .

[74] Z. C. Zeng, A. H. G. Peter, X. Du, S. Yang, A. Benson, F.-Y. Cyr-Racine, F. Jiang, C. Mace, and R. B. Metcalf, "Till the core collapses: the evolution and properties of self-interacting dark matter subhalos," (2023), arXiv:2310.09910 [astro-ph.GA] .

[75] W. Dehnen and J. I. Read, The European Physical Journal Plus **126** (2011), 10.1140/epjp/i2011-11055-3.

[76] A. A. Dutton and A. V. Macciò, Monthly Notices of the Royal Astronomical Society **441**, 3359–3374 (2014).

[77] S. Garrison-Kimmel, M. Rocha, M. Boylan-Kolchin, J. Bullock, and J. Lally, Mon. Not. Roy. Astron. Soc. **433**, 3539 (2013), arXiv:1301.3137 [astro-ph.CO] .

[78] M. Zemp, B. Moore, J. Stadel, C. M. Carollo, and P. Madau, Monthly Notices of the Royal Astronomical Society **386**, 1543 (2008), https://academic.oup.com/mnras/article-pdf/386/3/1543/3638656/mnras0386-1543.pdf .

[79] A. S. Eddington, MNRAS **76**, 572 (1916).

[80] L. Hernquist, Astrophys. J. **356**, 359 (1990).

[81] M. Miyamoto and R. Nagai, Publ. Astron. Soc. Jap. **27**, 533 (1975).

[82] N. J. Outmezguine, K. K. Boddy, S. Gad-Nasr, M. Kaplinghat, and L. Sagunski, Monthly Notices of the Royal Astronomical Society **523**, 4786–4800 (2023).

[83] D. Yang and H.-B. Yu, Journal of Cosmology and Astroparticle Physics **2022**, 077 (2022).

[84] Z.-Z. Li, D.-H. Zhao, Y. P. Jing, J. Han, and F.-Y. Dong, Astrophys. J. **905**, 177 (2020), arXiv:2008.05710 [astro-ph.CO] .

[85] X. Zhang, H.-B. Yu, D. Yang, and H. An, "Self-interacting dark matter interpretation of crater ii," (2024), arXiv:2401.04985 [astro-ph.GA] .

[86] X. Du *et al.*, Phys. Rev. D **110**, 023019 (2024), arXiv:2403.09597 [astro-ph.GA] .